Alexis Balayre

Future Position Prediction for Pressure Refuelling Port of Commercial Aircraft

School of Aerospace, Transport and Manufacturing
Computational and Software Techniques in Engineering

MSc
Academic Year: 2023–2024

Supervisors: Dr. Boyu Kuang and Dr. Stuart Barnes
August 2024

School of Aerospace, Transport and Manufacturing
Computational and Software Techniques in Engineering

MSc

Academic Year: 2023–2024

Alexis Balayre

Future Position Prediction for Pressure Refuelling Port of Commercial Aircraft

Supervisors: Dr. Boyu Kuang and Dr. Stuart Barnes
August 2024

This thesis is submitted in partial fulfilment of the requirements for the degree of MSc.

Academic Integrity Declaration

I declare that:

- the thesis submitted has been written by me alone.
- the thesis submitted has not been previously submitted to this university or any other.
- that all content, including primary and/or secondary data, is true to the best of my knowledge.
- that all quotations and references have been duly acknowledged according to the requirements of academic research.

I understand that to knowingly submit work in violation of the above statement will be considered by examiners as academic misconduct.

Abstract

This thesis presents the development of a robust and efficient framework for predicting the future position of the pressure refuelling port of commercial aircraft. The proposed framework addresses critical challenges in automated aircraft refuelling systems, where accurate detection and prediction of the refuelling port's position are essential for operational efficiency and safety. Leveraging deep learning techniques, the framework integrates a fine-tuned *YOLOv10* object detection model with a proposed sequence model, termed *SizPos-GRU*. This sequence model utilises an encoder-attention-decoder architecture to effectively capture temporal dependencies and spatial relationships from video frames. The methodology includes meticulous dataset configuration and annotation, followed by hyperparameter tuning to optimise model performance. Experimental results demonstrate the *SizPos-GRU* model's superior predictive accuracy across different scenarios. Specifically, the *Savitzky-Golay* filter combined with a *Linear Kalman Filter* (LKF) yielded the best performance, achieving an Average Displacement Error (ADE) of 32.45 pixels and a Final Displacement Error (FDE) of 57.98 pixels in the *video_lab_platform_6* dataset. Additionally, the model achieved a Final Intersection over Union (FIoU) of 28.27%, highlighting its ability to maintain spatial overlap between predicted and actual positions. In other datasets, such as *test_indoor1*, the framework demonstrated consistent performance with an ADE of 76.48 pixels and an FDE of 127.81 pixels when using the Savitzky-Golay filter without LKF. These findings underscore the potential of the proposed framework to significantly improve the automation of aircraft ground operations, making a valuable contribution to the field by advancing the state-of-the-art in predictive modelling for dynamic environments.

Keywords:
Aircraft Refuelling Port Detection, Spatio-temporal Prediction, Deep Learning Sequence Models, *SizPos-GRU* model, Kalman Filtering, Savitzky-Golay Smoothing

Acknowledgements

I would like to express my deepest gratitude to my supervisors, Dr. Boyu Kuang and Dr. Stuart Barnes, for their invaluable guidance, encouragement, and support throughout this research. I am especially grateful to Dr. Boyu Kuang, whose unwavering dedication, insightful feedback, and willingness to go the extra mile have been instrumental in overcoming the challenges faced during this study. His mentorship has not only greatly enriched the quality of this thesis but also inspired me to pursue excellence in my research. I also wish to acknowledge the use of ChatGPT, an AI language model by OpenAI, which provided assistance in refining the language and clarity of this thesis. As a non-native English speaker, this support was instrumental in ensuring the quality of the writing. I am also grateful to Dr. Muhammad Monjurul Karim, Postdoctoral Scholar at the University of Washington, for providing access to the source code of the Fusion-GRU model [39], which was pivotal in the development of this research. Additionally, I would like to extend my appreciation to Airbus, the UK Research and Innovation (UKRI) and the Aerospace Technology Institute (ATI) for sponsoring this research through the ONEheart project. Finally, my heartfelt thanks go to my family and friends for their unwavering support and understanding during my studies.

Table of Contents

List of Figures

List of Tables

List of Abbreviations

AAGR	Autonomous Aircraft Ground Refuelling
ADE	Average Displacement Error
AFRL	Air Force Research Laboratory
AI	Artificial Intelligence
AAR	Autonomous Aerial Refuelling
AIoU	Average Intersection over Union
AP	Average Precision
AR	Average Recall
AR3P	Autonomous & Robotic Remote Refuelling Point
CNN	Convolutional Neural Network
CV	Constant Velocity
DGPS	Differential Global Positioning System
DL	Deep Learning
EKF	Extended Kalman Filter
FDE	Final Displacement Error
FIoU	Final Intersection over Union
GPS	Global Positioning System
GRU	Gated Recurrent Unit
HOG	Histogram of Oriented Gradients
IoT	Internet of Things
IoU	Intersection over Union
LKF	Linear Kalman Filter
LSTM	Long Short-Term Memory
ML	Machine Learning
NMS	Non-Maximum Suppression
PV-LSTM	Pedestrian Intention Prediction LSTM
RNN	Recurrent Neural Network
SOTA	State-of-the-Art
SSD	Single Shot Multibox Detector
STED	Spatio-Temporal Encoder-Decoder
UAV	Unmanned Aerial Vehicle
YOLO	You Only Look Once

Chapter 1

Introduction

1.1 Background and Motivation

Ground pressure refuelling is a standard method used to refuel commercial aircraft safely and efficiently. This process involves using a system of underground fuel pipelines and hydrants at aircraft parking spots [8]. When an aircraft is ready for refuelling, a hydrant dispenser vehicle connects to the hydrant pit and delivers fuel to the aircraft through a flexible hose [58, 19] (see Figure 1.1). This method allows for high fuel flow rates and significantly reduces aircraft turnaround times [8]. However, this process also presents several challenges, particularly in terms of safety and accuracy. In the past, there have been several incidents involving ground pressure refuelling, including fuel spills, overfills, and equipment failures [51, 18]. Fortunately, with the advancement of technology, many of these challenges will be addressed, and the refuelling process will become safer and more efficient.

Figure 1.1: Pressure Refuelling of a Commercial Aircraft. Photo Credit: Tom Boon/Simple Flying [5]

The aviation industry is undergoing a significant transformation with the development of the airport of the future, commonly known as 'Smart Airport' or, more recently, 'Airport 4.0'. The concept of Smart Airport encompasses the use of cutting-edge information technologies, such as the Internet of Things (IoT), Artificial Intelligence (AI), and Blockchain, to monitor, analyse, and integrate real-time data on the airport's status. This integration aims to achieve optimal operational efficiency and enhance the quality of service. Taking the concept a step further, Airport 4.0 envisages an airport driven entirely by AI, capable of making autonomous decisions thanks to self-learning mechanisms. This advance aims to automatically predict and

manage various airport scenarios, making it easier to automate numerous processes. The result is a substantial reduction in operating costs and error rates [47].

Among these, automated refuelling systems play a crucial role in ensuring efficient and accurate refuelling of aircraft. However, one of the main challenges of this automation process is the accurate detection of the aircraft's refuelling port, which is relatively small and can easily be obscured by other visual elements on or near an aircraft. For example in the Figure 1.2, the refuelling port is located on the wing of the aircraft and can be difficult to detect due to motion blur, occlusion, or being out of view. This challenge is further compounded by the fact that aircraft refuelling ports can vary in size, shape, and location depending on the aircraft type and manufacturer. Scanning the entire area of each video frame is both time-consuming and inaccurate. It is therefore essential to develop a more efficient and accurate method of locating the refuelling port.

(a) Motion Blur Example (b) Occlusion Example (c) Out-of-View Example

Figure 1.2: Challenges in Detecting Aircraft Refuelling Port

1.2 Research Gap

Despite significant advancements in autonomous aircraft ground refuelling technologies, critical challenges remain, particularly in the accurate detection and positioning of the refuelling port. The small size and varied locations of refuelling ports, often obscured by visual elements like motion blur and occlusions, complicate this task. Existing systems have made progress using machine vision, but they are limited by inefficiencies in scanning entire video frames and inaccuracies under different environmental conditions. Furthermore, while current methodologies leveraging convolutional neural networks (CNNs) and Kalman filters have improved detection accuracy, they still struggle with real-time performance and adaptability in dynamic environments. The robustness of these systems in varied lighting conditions and their capability to handle different refuelling port types and obstructions need enhancement. Additionally, the application of advanced deep learning models like Long Short-Term Memory (LSTM) networks, Gated Recurrent Units (GRUs), and Transformers in this context is underexplored.

1.3 Aim and Objectives

This thesis aims to address the previous research gaps by developing a framework for predicting the future position of commercial aircraft refuelling ports using advanced Object Detection models and Deep Learning to leverage the spatial-temporal relationship between frames in a video.

1. Conduct a comprehensive review of state-of-the-art methods for Object Detection, Object Tracking, and Deep Learning Sequence Models.
2. Annotate and preprocess video datasets of aircraft refuelling ports to ensure high-quality training and testing data.
3. Design and develop a framework for accurately tracking and predicting the future position of aircraft refuelling ports.

1.4 Technological Contributions

This thesis presents significant technological contributions that advance the field of automated aircraft refuelling and predictive modelling. The primary contribution is the development of the *SizPos-GRU* model, a novel deep learning sequence model designed to accurately predict the future positions of aircraft refuelling ports in dynamic video sequences. The *SizPos-GRU* model employs an encoder-attention-decoder architecture that effectively captures temporal dependencies and spatial relationships from video frames, resulting in superior predictive accuracy when compared to existing models. In addition to this, the integration of a fine-tuned YOLOv10 object detection model with the *SizPos-GRU* framework provides a comprehensive solution for detecting, tracking, and predicting the future trajectory of the refuelling port. This integration not only enhances detection accuracy but also ensures robust trajectory prediction, which is critical for improving operational efficiency in automated refuelling systems. Furthermore, the thesis implements advanced smoothing techniques, including the Savitzky-Golay filter combined with Kalman Filters, to enhance the stability and reliability of predictions. These techniques are instrumental in filtering out noise and delivering smoother, more accurate predictions in real-world scenarios. These contributions collectively provide a robust and accurate framework for automating aircraft refuelling systems, with potential applications extending to various dynamic environments within the aerospace industry.

1.5 Thesis Layout

The following sections of this thesis provide a detailed exploration and analysis of the methodologies, experiments, and findings related to the development of an advanced framework for predicting the future positions of aircraft refuelling ports. Chapter 2 (Literature Review) presents an overview of the current state-of-the-art methods in automated aircraft refuelling systems, object detection, and deep learning for spatio-temporal prediction. Chapter 3 (Methodology) describes the step-by-step approach taken in dataset preparation, framework design, and model training. Chapter 4 (Experiment Design) outlines the experimental setups and comparison studies conducted to evaluate the performance of the proposed models. In the Chapter 5 (Results and Discussion), the outcomes of these experiments are presented and analysed, offering insights into the effectiveness and implications of the research findings. Finally, the Chapter 6 (Conclusion and Future Work) summarises the key contributions of the thesis, reflects on the significance of the results, and proposes directions for future research to further advance the field of automated aircraft refuelling systems.

Chapter 2

Literature Review

2.1 Automated Refulling Systems in the Aviation Industry

Ground refuelling operations are essential to maintaining aircraft availability and operational efficiency. The transition from manual to automated systems is designed to improve the safety, efficiency and reliability of these operations [53]. The concept of Autonomous Aircraft Ground Refuelling (AAGR) emerged in the 1980s in the United States to address the US Air Force's need to protect ground personnel from potential threats during refuelling operations [61]. In the early 1990s, Bennett et al. [7] introduced the Brightness Invariant Port Recognition System (BIPRS), marking a significant advancement in machine vision systems for identifying aircraft refuelling ports. In 2010, the Air Force Research Laboratory (AFRL) showcased the world's first Automated Aircraft Ground Refuelling system prototype through a video demonstration. This system featured a robot equipped with a fuel nozzle and a single-point refuelling adapter, enabling autonomous engagement with the aircraft's refuelling panel, as illustrated in Figure 2.1 [11]. This project will give birth to the Autonomous & Robotic Remote Refuelling Point (AR3P) project.

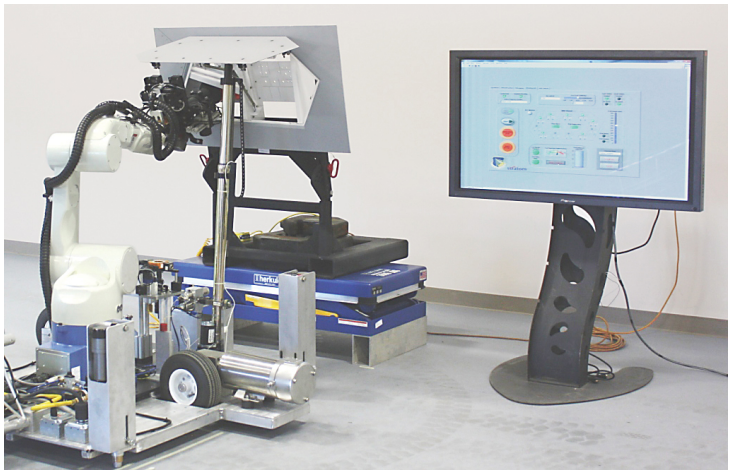

Figure 2.1: AFRL's Automated Aircraft Ground Refuelling system prototype robot (Photo Credit: AFRL/RXQ Robotics Group)

The Autonomous & Robotic Remote Refuelling Point (AR3P) project, developed by the U.S. Army, represents a pioneering initiative in unmanned refuelling operations for rotary-wing aircraft. This project leverages advanced robotics, including self-aligning mechanisms

and articulated arms equipped with sensors, to facilitate rapid and safe refuelling processes on non-contiguous battlefields. The AR3P system minimises the time aircraft spend on the ground and enhances safety by reducing soldier exposure at fueling stations. Initially demonstrated in a Limited Initial Capabilities event, the AR3P aims to meet the evolving range and endurance requirements of Army Aviation. The project integrates existing technologies with novel systems designed in-house, supported by commercial off-the-shelf components and additive manufacturing. Currently, AR3P is progressing through its development phases, addressing technical risks, and preparing for further testing and eventual deployment, as shown in Figure 2.2 [26].

Figure 2.2: AR3P Concept Development Prototype Robot (Photo Credit: U.S. Army)

The AR3P project exemplifies the intersection of advanced robotics and practical military applications, highlighting the potential of automated systems to transform operational paradigms. Figure 2.3 provides visual insights into the capabilities of the AR3P system, by performing autonomous hot refuelling. During this test, the robot is equipped with a LIDAR sensor and a camera to detect the aircraft's refuelling port. In Figure 2.3a, the AR3P robot is seen approaching a detected aircraft, demonstrating its autonomous navigation and alignment capabilities. In Figure 2.3b, the AR3P robot is shown engaging the aircraft refuelling port, emphasising its precision and functionality in connecting to the aircraft's fuel port. These images illustrate the practical implementation of robotic technologies in enhancing the safety, efficiency, and speed of refuelling operations, particularly in challenging and hazardous environments [4].

(a) AR3P Robot Approaching Detected Aircraft (Photo Credit: Stratom)

(b) AR3P Robot Engaging Aircraft Refuelling Port (Photo Credit: Stratom)

Figure 2.3: AR3P Robot Hot Refuelling Demonstration for S-70 Helicopter

Unfortunately, there is very little literature on existing AAGR systems, as most research is carried out by the military and is classified. The most recent papers cover Autonomous Aerial Refuelling (AAR) systems, which are used to refuel unmanned aerial vehicles (UAVs) in mid-air. These systems are designed to extend the flight time and range of UAVs by enabling them to refuel without landing. AAR systems are particularly challenging due to the high speeds and altitudes involved, as well as the need for precise measurement and tracking of the relative position between the receiver aircraft and the tanker aircraft are critical, particularly during the docking phase (see figure 2.4) [31, 69, 14]. Zhong et al. [80] propose a robust solution that utilises monocular vision combined with an extended Kalman filter (EKF) [12] to address this challenge. By implementing EKF, the system can provide reliable position estimations and track the drogue within a specified region of interest (ROI), even in the presence of disturbances such as air turbulence. As shown in figure 2.5, this system initialises the state and covariance matrices, predicts the drogue's position, updates the state based on new measurements, and continuously refines the ROI for subsequent image processing. This approach significantly reduces the processing time and improves the detection frequency from 10 Hz to up to 30 Hz by focusing computational resources on the predicted ROI.

Figure 2.4: Autonomous Aerial Refuelling (AAR) of X-47B Unmanned Combat Air System Demonstrator (Photo Credit: U.S. Navy)

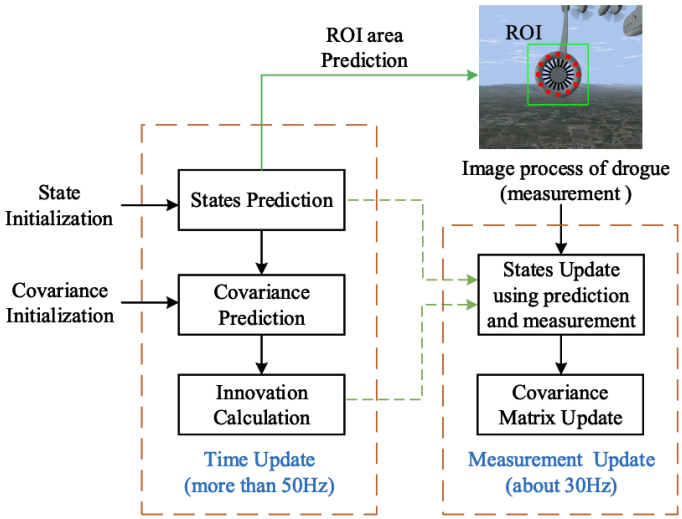

Figure 2.5: Autonomous Air Refuelling Detection System with EKF. Source: Zhong et al. [80]

Recent advancements in autonomous ground refuelling have been driven by improvements in computer vision and robotics. Yildirim et al. [76] presented the PosEst system, which combines 2D RGB images with 3D point cloud data to enhance detection accuracy. This system

uses a custom-trained EfficientNet-B0 CNN for object detection and leverages the Kalman filter for stable 3D pose estimation (see Figure 2.6). The PosEst method employs a dual approach of high-precision detection and robust tracking. By predicting and updating the object's state in real-time, the Kalman filter facilitates continuous and precise alignment of the fuel nozzle with the refuelling adaptor, even in dynamic environments. This approach significantly reduces the risks associated with manual refuelling and improves operational efficiency and safety.

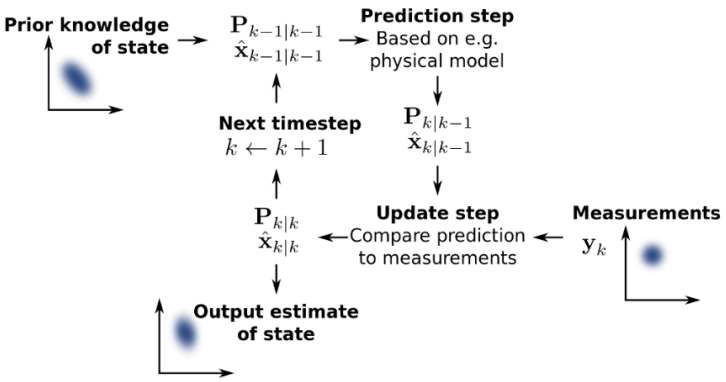

Figure 2.6: Kalman Filter Workflow for Pose Estimation in Autonomous Ground Refuelling. Source: Yildirim et al. [76]

One of the primary challenges in AAGR is the accurate detection and positioning of the refuelling port under varying environmental conditions. Robust datasets for scene recognition and machine learning applications have been developed to address these challenges. Kuang et al. [41] introduced a comprehensive dataset for AAGR, addressing significant challenges such as variant illumination conditions, different refuelling port types, and environmental obstructions. The dataset comprises over 26,000 labeled images collected through image crawling from 13 different databases, followed by augmentation to ensure diversity (see Figure 2.7). Additionally, recent innovations have introduced hybrid datasets combining real and synthetic data for training and validating systems [77, 75]. This approach offers a wide range of scenarios and conditions, improving the robustness and accuracy of automated refuelling systems. The development of high-quality datasets is pivotal in improving the robustness and reliability of AAGR systems.

Figure 2.7: AAGR Dataset Overview. Source: Kuang et al. [41]

2.2 Object Detection and Tracking in Computer Vision

In Computer Vision, Object Detection refers to the identification and location of individual objects within an image, providing both spatial information (bounding boxes) and confidence scores, which represent the probability that each detected object belongs to the predicted class [22]. For example, in the following image, there are five detections, including one 'ball' with a confidence level of 98% and four 'people' with confidence levels of 98%, 95%, 97% and 97%. Evaluating Object Detection models involves several key metrics to measure their performance. One common metric is Intersection over Union (IoU), which measures the overlap between a predicted bounding box and a ground-truth bounding box, as shown in Figure 2.9.

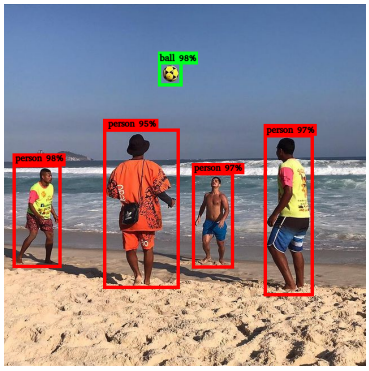

Figure 2.8: Example of outputs from an object detector [22].

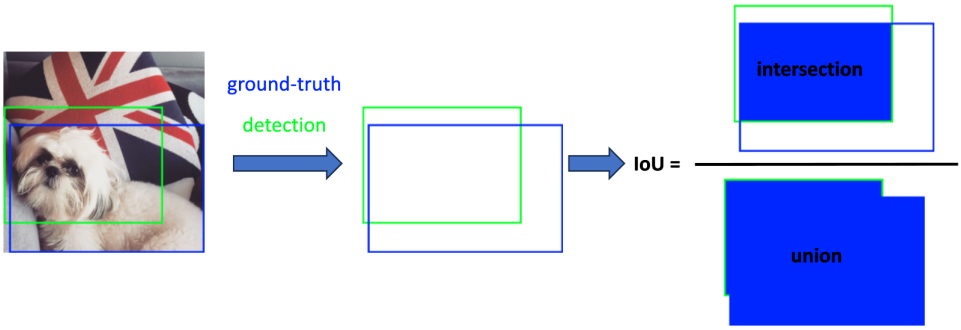

Figure 2.9: Intersection over Union (IoU) between a detection (in green) and ground-truth (in blue). [22]

Over the last few decades, Object Detection models based on Deep Learning have enjoyed remarkable success. These models fall into two main categories: two-stage detectors and single-stage detectors. On the one hand, two-stage detectors, such as R-CNN [30], Fast R-CNN [29], Faster R-CNN [57], R-FCN [20], and DETR [13], first generate region proposals and then refine these proposals into precise anchor boxes. While these models excel in detection accuracy, they typically suffer from large model sizes and slower detection speeds [37, 74]. On the other hand, single-stage detectors, including the SSD (Single Shot Multibox Detector) [49], YOLO (You Only Look Once) series [56, 55, 9, 16, 27, 33, 45, 34, 68, 71, 67, 72, 66], and RetinaNet [46] directly predict object locations and categories in a single network pass. These models are known for their high detection speeds but sometimes compromise accuracy [37, 74, 21].

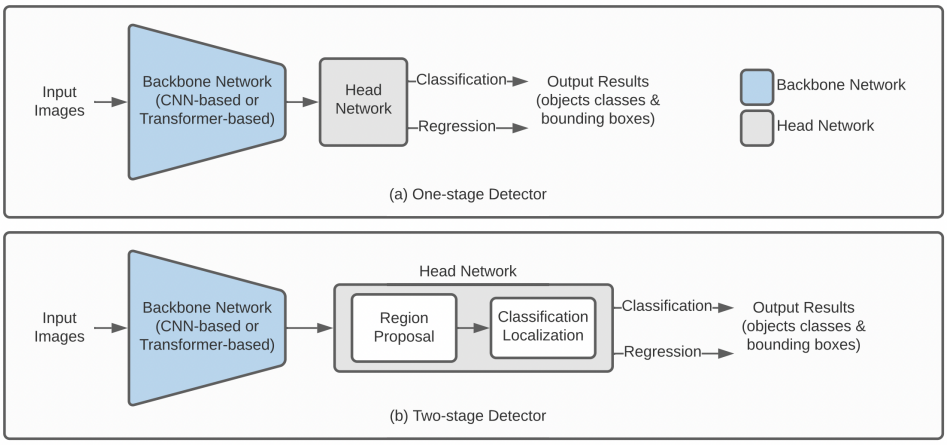

Figure 2.10: Basic deep learning-based one-stage vs two-stage object detection model architectures [37].

YOLOv10, the latest iteration in the YOLO series, marks a significant leap forward in real-time object detection with the introduction of NMS-free training. Traditionally, single-stage detectors relied on Non-Maximum Suppression (NMS) during post-processing to eliminate redundant predictions, as illustrated in Figure 2.11. However, this process can sometimes be overly aggressive, risking the loss of valuable predictions or failing to remove all duplicates effectively, which also adds to computational costs during both training and inference [28].

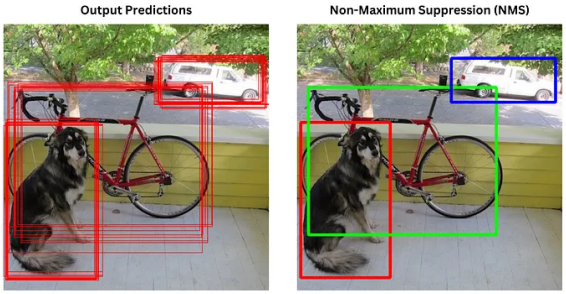

Figure 2.11: Non-Maximum Suppression (NMS) in Object Detection [28].

YOLOv10 overcomes these limitations by implementing a consistent dual assignments strategy that facilitates NMS-free training. This strategy leverages both one-to-many and one-to-one label assignments during training, providing the model with rich supervision while enabling efficient end-to-end deployment. During inference, the one-to-one assignment head is employed, which eliminates the need for NMS and significantly reduces inference time. As depicted in Figure 2.12, the one-to-many head assigns multiple labels to each anchor box, enriching the model's supervision, while the one-to-one head refines these predictions by assigning a single label to each anchor box, ensuring precise and efficient detection [66].

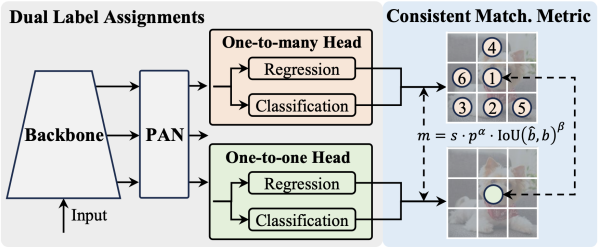

Figure 2.12: YOLOv10 Model Workflow [66]

In addition, YOLOv10 adopts a holistic efficiency-accuracy driven design that optimises the model's architecture across various dimensions. The classification head has been redesigned to be more lightweight, reducing computational overhead while maintaining accuracy. The spatial-channel decoupled downsampling technique separates spatial reduction and channel increase operations, which lowers computational costs and reduces the parameter count. Furthermore, the rank-guided block design minimises redundancy within the model by adapting the complexity of different stages based on their intrinsic rank values, ensuring optimal capacity-efficiency trade-offs. YOLOv10 also introduces large-kernel (see figure 2.13) convolutions selectively in the deeper stages of the network to increase the receptive field, allowing the model to capture more contextual information without a significant increase in computational cost. Moreover, YOLOv10 incorporates a partial self-attention (PSA) mechanism, which integrates the benefits of global context modelling while maintaining a lightweight architecture. This careful balance of efficiency and accuracy enables YOLOv10 to deliver state-of-the-art performance [66, 28].

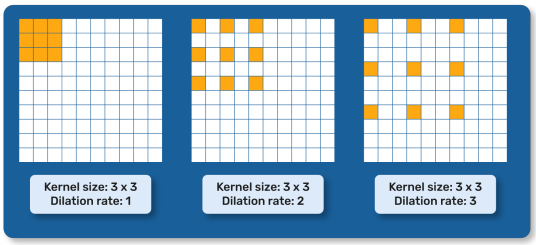

Figure 2.13: Large-Kernel Convolution in YOLOv10 [28]

As shown in Table 2.1, extensive testing on standard benchmarks, such as COCO, demonstrates YOLOv10's superior performance in both speed and accuracy. For example, YOLOv10-S is 1.8 times faster than RT-DETR-R18 while also using fewer parameters. Similarly, YOLOv10-B achieves a 46% reduction in latency compared to YOLOv9-C without compromising performance. These results underscore YOLOv10's effectiveness as a real-time end-to-end object detection model, making it well-suited for applications requiring both high speed and accuracy.

Table 2.1: Performance Comparison of YOLO Models with State-of-the-Art Techniques [66].

Model	Params (M)	FLOPs (G)	AP_{val} (%)	Latency (ms)
YOLOv6-3.0-N	4.7	11.4	37.0	2.69
Gold-YOLO-N	5.6	12.1	39.6	2.92
YOLOv8-N	3.2	8.7	37.3	6.16
YOLOv10-N	**2.3**	**6.7**	**39.5**	**1.84**
YOLOv6-3.0-S	18.5	45.3	44.3	3.42
Gold-YOLO-S	21.5	46.0	45.4	3.82
YOLO-MS-XS	4.5	17.4	43.4	8.23
YOLO-MS-S	8.1	31.2	46.2	10.12
YOLOv8-S	11.2	28.6	44.9	7.07
YOLOv9-S	7.1	26.4	46.7	-
RT-DETR-R18	20.0	60.0	46.5	4.58
YOLOv10-S	**7.2**	**21.6**	**46.8**	**2.49**
YOLOv6-3.0-M	34.9	85.8	49.1	5.63
Gold-YOLO-M	41.3	87.5	49.8	6.38
YOLO-MS	22.2	80.2	51.0	12.41
YOLOv8-M	25.9	78.9	50.6	9.50
YOLOv9-M	20.0	76.3	51.1	-
RT-DETR-R34	31.0	92.0	48.9	6.32
RT-DETR-R50m	36.0	100.0	51.3	6.90
YOLOv10-M	**15.4**	**59.1**	**51.3**	**4.74**

In addition to Object Detection, Object Tracking is another critical task in Computer Vision, involving the continuous monitoring of objects across video frames. Object Tracking methods can be broadly classified into two categories: **Generative Trackers** and **Discriminative Trackers** [15]. Generative trackers are capable of handling challenging scenarios such as occlusion and large-scale variation through particle sampling strategies, often integrated with various appearance models, including sparse representation and energy of motion. Discriminative trackers, by contrast, build robust classifiers using hand-crafted or deep features [15]. The combination of generative and discriminative approaches, as well as the integration of deep learning techniques such as fully revolutionary networks and Transformer models, has led to significant improvements in object detection performance [48, 79, 78]. In addition, the speed and computational requirements of these algorithms are critical factors influencing their practical applicability [79, 78, 42]. Advanced techniques in object tracking leverage both generative and discriminative models to amplify tracking efficacy. The utilisation of deep trackers has evidenced superior results on public tracking datasets, attributed to their potent feature extractors, accurate bounding box regressors, and discriminative classifiers [42]. Techniques such as deformable convolution and Transformer models extend traditional convolution or correlation methodologies to execute global feature matching, thereby enhancing tracking accuracy. The incorporation of contextual or knowledge information can substantially elevate performance, with methodologies like Particle Filtering, also recognised as Sequential Monte Carlo (SMC) methods, framed as problems of Bayesian inference in state space [17, 70]. The extended Kalman Filtering (EKF) is another advanced technique that has been employed to improve tracking accuracy by predicting the current status through the previous status and modifying the prediction result based on observation information [79, 78]. Despite these advancements, the integration of these methods in a complementary manner remains an open research area with substantial potential for advancing the field [48, 79].

2.3 Deep Learning for Spacio-Temporal Prediction

Time series prediction involves processing sequential data to predict future events or values. Various deep learning models have been applied to this task, requiring several preparatory steps such as collecting data, designating attribute types, dealing with inconsistencies and storing datasets. These datasets are usually classified into units of time such as seconds, minutes and hours, allowing the construction of metadata for machine learning [44].

State-of-the-Art Sequence Models

The prediction of future object locations has been a critical focus of research, particularly in autonomous driving and surveillance applications. Early approaches to this problem primarily utilised Recurrent Neural Networks (RNNs), which include Long Short-Term Memory networks (LSTMs) and Gated Recurrent Units (GRUs) [2, 6, 43, 25, 52]. These models employ an encoder-decoder architecture to encode sequences of past observations and decode future locations. The encoder processes the input sequence to capture temporal dependencies, while the decoder predicts the future sequence based on the encoded information. RNNs, especially LSTMs and GRUs, have shown significant potential in sequence prediction tasks due to their ability to model long-term dependencies [24, 62, 64]. However, these models often suffer from performance degradation over time, primarily because they recursively predict future bounding boxes based on the previous outputs, which can lead to error accumulation [39]. To address these limitations, early models incorporated additional contextual inputs, such as environmental data and semantic actions, to improve prediction accuracy. For example, Alahi et al. [1] introduced the Social-LSTM model, which accounts for the interactions between pedestrians, using a social pooling mechanism to enhance global context understanding and improve trajectory predictions. As depicted in Figure 2.14, the key differences between RNN, LSTM, and GRU models lie in their internal architectures and mechanisms for handling information flow over time. LSTMs and GRUs are designed to mitigate the vanishing gradient problem commonly associated with standard RNNs by incorporating gating mechanisms. These gates control the flow of information, allowing the model to retain or forget certain information as needed, thereby improving its ability to capture long-term dependencies.

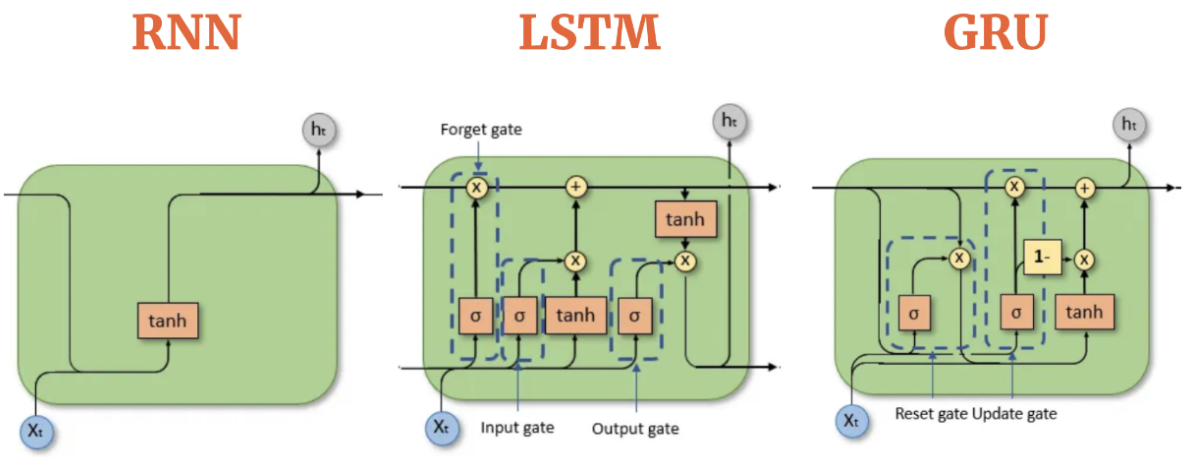

Figure 2.14: Comparing different Sequence models: RNN, LSTM, and GRU. Source: Colah's blog. Compiled by AIML.com

Use of LSTMs and GRUs in Sequence Prediction

Spatio-Temporal Encoder-Decoder (STED) Model

The STED model was introduced by Styles et al. [65] as a novel approach for multiple object forecasting (MOF), particularly in predicting the future bounding boxes of tracked objects from video sequences. This model is designed to handle the challenges of object forecasting in diverse environments, leveraging both visual and temporal features to predict object-motion and ego-motion effectively. As shown in Figure 2.15, the STED model consists of three main components: a bounding box feature encoder, an optical flow feature encoder, and a decoder. The *Bounding Box Feature Encoder* utilises a Gated Recurrent Unit (GRU) to extract temporal features from past object bounding boxes, which include coordinates (x, y), dimensions (w, h), and velocity changes $(\Delta x, \Delta y, \Delta w, \Delta h)$ over a window of 30 frames, representing 1 second of observation. Simultaneously, the *Optical Flow Feature Encoder* captures motion features directly from optical flow, using a Convolutional Neural Network (CNN) to process a stack of 10 frames sampled uniformly from the past 1 second of video data. The combination of these features provides a comprehensive understanding of both the object's movement and the camera's movement (ego-motion). The *Decoder* then takes the concatenated feature vector from the encoders and predicts the future bounding box coordinates for the next 60 frames (2 seconds prediction window). The GRU-based decoder generates bounding box predictions iteratively, using the encoded feature vector and the internal hidden state to output changes in bounding box velocity and dimensions over time.

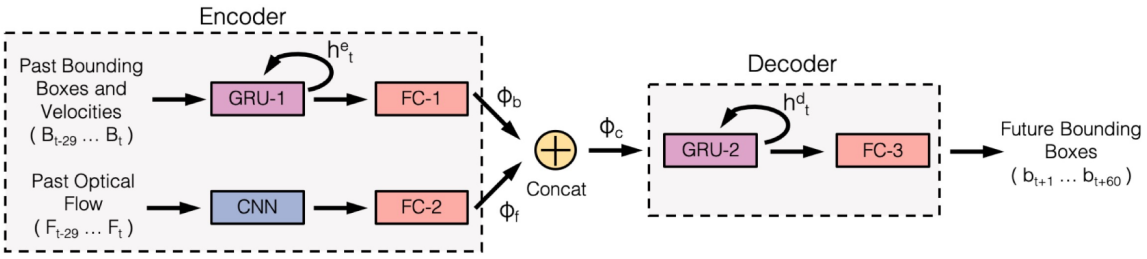

Figure 2.15: STED Model Architecture. Source: Styles et al. [65]

The STED architecture is specifically designed to address the complexities of predicting future object positions in video sequences, particularly under conditions of non-linear object motion and varying scales due to camera movement. By combining temporal features from bounding boxes with motion information from optical flow, the model effectively captures both the dynamic behaviour of the objects and the impact of the camera's motion on the observed scene. The STED model was evaluated on the Citywalks dataset [65], a diverse dataset designed to test the model's ability to predict future object locations across different environments. The performance of STED was compared with several baseline models, as summarised in Table 2.2. Metrics include Average Displacement Error (ADE), Final Displacement Error (FDE), Average Intersection-over-Union (AIoU), and Final Intersection-over-Union (FIoU). The model was evaluated using 1 second of input frames to predict 2 seconds of future frames.

Table 2.2: Comparison of the performance of STED with baseline models on the Citywalks dataset.

Model	ADE (pixels)	FDE (pixels)	AIoU (%)	FIoU (%)
CV-CS [65]	31.6	57.6	46.0	21.3
LKF [65]	32.9	59.0	43.9	20.1
STED [65]	**26.0**	**46.9**	**51.8**	**27.5**

The STED model achieved an Average Displacement Error (ADE) of 26.0 pixels and a Final Displacement Error (FDE) of 46.9 pixels, with an Average Intersection Over Union (AIoU) of 51.8% and a Final Intersection Over Union (FIoU) of 27.5%. These results indicate that STED outperforms existing models in both displacement and intersection-over-union metrics, making it a robust solution for forecasting future object locations in challenging video sequences.

Position-Velocity Long Short-Term Memory (PV-LSTM) Model

The PV-LSTM model was developed by Bouhsain et al. [10] to predict pedestrian intentions and future bounding box positions, a crucial task for enhancing the safety of autonomous driving systems. The architecture of this model is illustrated in Figure 2.16. The model utilises a sequence-to-sequence LSTM architecture that processes both spatial and temporal information effectively. To do that, it processes input sequences of observed bounding boxes (x, y, w, h) and their velocity changes $(\Delta x, \Delta y, \Delta w, \Delta h)$ over a window of 30 frames, representing 1 second of observation. These inputs are encoded through two encoders: the *Bounding Box Position Encoder* and the *Bounding Box Velocity Encoder*. The encoded features are then concatenated and passed to two decoders: the *Velocity Decoder*, which predicts future bounding box velocities, and the *Intention Decoder*, which predicts pedestrian crossing intentions over the next 60 frames (2 seconds prediction window). The PV-LSTM model's architecture is designed to capture the dynamic and complex nature of pedestrian behaviour, which is crucial for real-time decision-making in autonomous driving. By integrating both position and velocity information through dual encoders, the model can more accurately predict the future movements and intentions of pedestrians, thus enhancing safety and reliability in autonomous navigation systems.

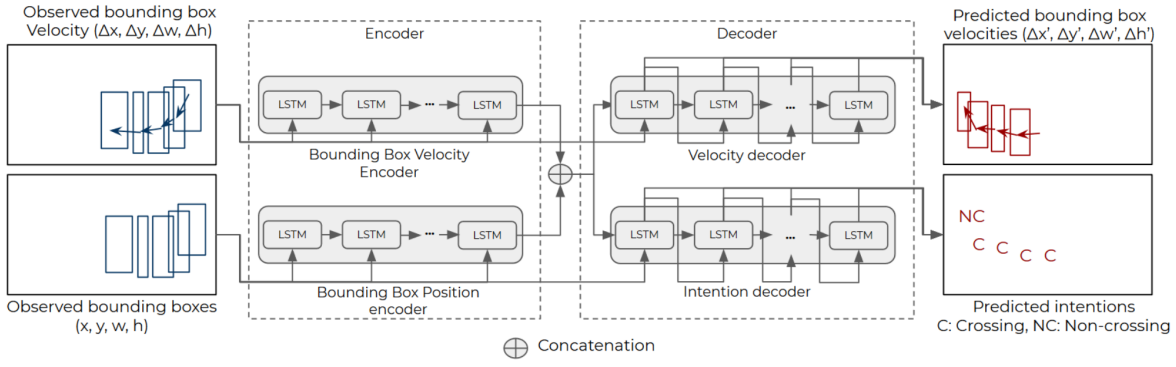

Figure 2.16: PV-LSTM Model Architecture. Source: Bouhsain et al. [10]

The PV-LSTM model was evaluated on the Citywalks dataset, and its performance was compared against several baseline models. The results are summarised in Table 2.3, showcasing the model's effectiveness in predicting pedestrian trajectories and intentions. The PV-LSTM model

achieved an Average Displacement Error (ADE) of 25.2 pixels and a Final Displacement Error (FDE) of 49.9 pixels, with an Average Intersection Over Union (AIoU) of 40.2%. Although the STED model slightly outperforms in AIoU and FIoU, the PV-LSTM model provides a robust solution with competitive prediction accuracy, while maintaining a simpler architecture.

Table 2.3: Comparison of the performance of PV-LSTM with baseline models on the Citywalks dataset.

Model	ADE (pixels)	FDE (pixels)	AIoU (%)	FIoU (%)
CV-CS [10]	31.6	57.6	46.0	21.3
LKF [10]	32.9	59.0	43.9	20.1
STED [10]	**26.0**	**46.9**	**51.8**	**27.5**
PV-LSTM [10]	25.2	49.9	40.2	20.3

Fusion-Gated Recurrent Unit (Fusion-GRU) Model

Karim et al. [39] developed the Fusion-Gated Recurrent Unit (Fusion-GRU) model to predict the future bounding boxes of traffic agents in risky driving scenarios. As illustrated in Figure 2.17, this model leverages multiple sources of information, such as location-scale data, monocular depth information, and optical flow data, to capture complex interactions among these cues and transform them into meaningful hidden representations. This approach is particularly suited for dealing with scenarios where the available observation time is limited due to abrupt motion changes or tracking loss. The Fusion-GRU model consists of several components that work together to predict future bounding boxes. The model takes input video sequences, extracts depth maps, and calculates optical flow to capture motion dynamics. Bounding boxes are detected and tracked using YOLOv5 and DeepSort, respectively. The feature extractor processes both object-level and scene-level features using ResNet50, transforming them into feature vectors. These vectors are then concatenated and passed to the Fusion-GRU encoder, which integrates location, scale, and distance information into hidden representations. The model also introduces an intermediary estimator, which generates intermediate bounding boxes that help in capturing sequential dependencies across frames. Additionally, a self-attention aggregation layer is employed to reduce error accumulation by focusing on the most relevant information for long-term predictions. Finally, a GRU decoder iteratively predicts the future bounding boxes based on the aggregated feature vectors and the hidden representations from the Fusion-GRU encoder.

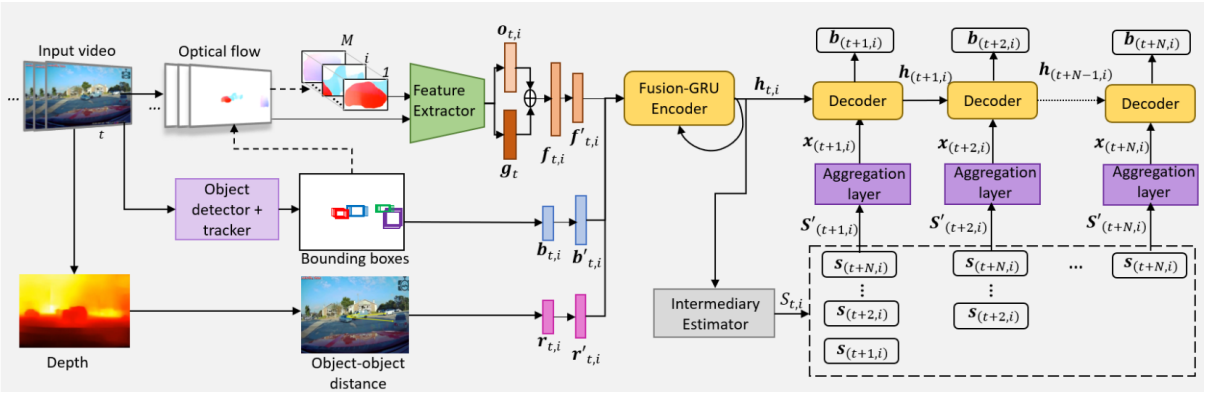

Figure 2.17: Fusion-GRU model architecture. Source: Karim et al. [39]

The Fusion-GRU model is specifically designed to address the limitations of traditional GRU-based models, which often suffer from performance degradation over time. By integrating complex interactions among various input features and employing self-attention mechanisms, the Fusion-GRU model enhances its ability to predict future bounding boxes more accurately. This architecture is particularly effective in cluttered and dynamic driving environments, where understanding the relationships between different traffic agents and their surroundings is crucial for accurate prediction. The Fusion-GRU model was evaluated on two publicly available datasets, ROL (Risky Object Localization) [38] and HEV-I (Honda Egocentric View-Intersection) [73, 50], demonstrating its superior performance in predicting future bounding boxes compared to other state-of-the-art models. The results are summarised in Table 2.4, which compares the performance of Fusion-GRU with baseline models based on metrics such as Average Displacement Error (ADE), Final Displacement Error (FDE), and Intersection over Union (IOU). The Fusion-GRU model achieved the lowest Average Displacement Error (ADE) and Final Displacement Error (FDE) in both 0.5-second and 1-second prediction horizons on the HEV-I dataset. It also exhibited the highest Final Intersection over Union (FIoU) of 85.2% in the 0.5-second horizon, indicating its strong capability to accurately predict the future positions and scales of traffic agents.

Table 2.4: Comparison of the performance of Fusion-GRU with baseline models on the ROL and HEV-I datasets.

Model	**ADE0.5 (pixels)**	**FDE0.5 (pixels)**	**FIoU0.5 (%)**	**ADE1.0 (pixels)**
FOL-X [39]	6.7	11.0	85.0	12.6
SGDNet [39]	6.3	–	–	11.4
Fusion-GRU [39]	**5.5**	**8.3**	**85.2**	**11.2**

Chapter 3

Methodology

3.1 Dataset Configuration

3.1.1 Dataset Description

The 'Airbus A320 Refuelling Port' (AARP) dataset consists of 21 video sequences captured inside or nearby an indoor hangar at the Aerospace Integration Research Centre (AIRC). This dataset can be utilised for various purposes, including but not limited to refuelling port detection and tracking, camera pose estimation, and visual image processing. It is provided under the terms of the UKRI funding agreement, as part of the ONEHeart project which aims to develop an automated aircraft refuelling system based on computer vision and robotics technology. Unauthorised use, distribution, or reproduction is prohibited. The AARP dataset consists of 21 video sequences captured in an indoor hangar at the Aerospace Integration Research Centre (AIRC). The videos were recorded using an Intel® RealSense™ D435 [32] (Shown in Figure 3.1), which provides depth information in addition to RGB data. The target area for detection and tracking is near the refuelling port of an Airbus A320 wing. The videos were recorded under different lighting conditions, including indoor artificial lighting and natural daylight, to simulate real-world scenarios. In addition, the refuelling port was in different states (closed, open, and semi-open) to capture a wide range of variations for training and testing machine learning models.

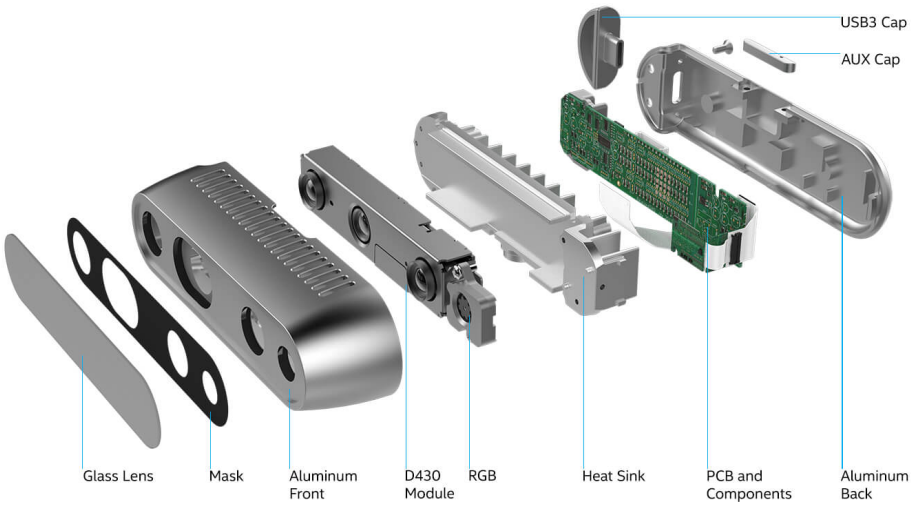

Figure 3.1: Intel® RealSense™ D435 Depth Camera. Source: Intel

3.1.2 Data Annotation

The AARP dataset provided for this project was not fully annotated. Therefore, the first step in the data preparation process was to annotate the dataset. This annotation process was crucial to enable the training of machine learning models for accurate refuelling port detection and tracking. Initially, 100 frames from each video sequence were manually annotated. This involved labeling the refuelling port in each frame, which required identifying and marking the exact location of the refuelling port using bounding boxes. This was done using the Label Studio tool, a powerful annotation platform that allows users to create and manage annotations in images and videos. Label Studio was chosen for its flexibility and ease of use. It supports various annotation formats and integrates well with machine learning workflows. Users can draw bounding boxes around objects of interest, in this case, the refuelling port, to create labeled datasets. The initial manual annotations created a preliminary dataset. This dataset was used to train a YOLOv10 (You Only Look Once, version 10) model for refuelling port detection. The annotated dataset was used to train the YOLOv10 model. The model learned to detect the refuelling port from the annotated images, improving its accuracy with each training iteration. After training the YOLOv10 model, it was implemented as a backend service for Label Studio. This was deployed as a Docker container, allowing the model to be used for automated annotation of the remaining images in the dataset. The model predicted the location of the refuelling port in new frames, and these predictions were used to annotate the rest of the dataset automatically. Each automatically generated annotation was reviewed manually to ensure accuracy. This review process involved verifying the location of the refuelling port in each frame and making necessary corrections to the annotations. This thorough quality control ensured that the entire dataset was consistently and accurately labeled. This comprehensive annotation process ensured that the entire dataset was accurately labeled, providing a robust foundation for training machine learning models aimed at refuelling port detection and tracking. The combination of manual and automated annotation techniques maximised efficiency while maintaining high annotation quality.

3.1.3 Summary of Available Videos

Each video was assigned to a specific dataset (train, val, and test), with an approximate split of 70% for training, 15% for validation, and 15% for testing. Table 3.1 presents the available videos in the dataset along with the number of frames for each video and their assignment:

Type	Video Name	Number of Frames	Assignment
Closed	**video_lab_platform_1**	**624**	**train**
Closed	video_lab_platform_2	639	train
Closed	video_lab_platform_5	398	train
Closed	video_lab_platform_7	412	train
Closed	video_lab_platform_8	470	train
Closed	video_lab_platform_9	373	train
Closed	video_lab_manual_1	746	train
Closed	video_lab_platform_3	569	val
Closed	video_lab_platform_4	247	val
Closed	video_lab_platform_6	303	test
Closed	test_outdoor1	499	test
Open	**video_lab_open_1_____1**	**497**	**train**
Open	video_lab_open_1_____2	602	train
Open	video_lab_open_1_____3	313	train
Open	video_lab_open_1_____4	310	train
Open	test_indoor2	310	val
Open	test_indoor1	314	test
Semi-Open	**video_lab_semiopen_1_____1**	**739**	**train**
Semi-Open	video_lab_semiopen_1_____2	439	train
Semi-Open	video_lab_semiopen_1_____4	372	val
Semi-Open	video_lab_semiopen_1_____3	383	test

Table 3.1: Summary of available videos in the AARP dataset with their assignment.

3.1.4 Data Distribution

Before balancing the data, the distribution of video frames across the different datasets (train, validation, and test) for each state of the fueling port (CLOSED, OPEN, and SEMI-OPEN) was as follows:

Type	Total Frames	Train	Test	Validation
CLOSED	5280	3662 (69.36%)	802 (15.19%)	816 (15.45%)
OPEN	2346	1722 (73.40%)	314 (13.38%)	310 (13.21%)
SEMI-OPEN	1933	1178 (60.94%)	383 (19.81%)	372 (19.24%)

Table 3.2: Distribution of frames across train, test, and validation sets for each state in the AARP dataset before balancing.

As shown in Table 3.2, the dataset initially had an imbalance in the number of frames for each state. For instance, the CLOSED state had significantly more frames compared to the OPEN and SEMI-OPEN states. This imbalance could lead to biased training and inaccurate model performance, as the model might become overly familiar with the more prevalent CLOSED state and underperform on the less represented states.

3.1.5 Data Balancing

To address this issue, a balancing strategy was employed to create a more uniform dataset. The first step involved shuffling and subsetting each state (CLOSED, OPEN, and SEMI-OPEN) to keep only the minimum number of frames for each state. This ensured that the number of frames for each state was equal, avoiding bias towards any particular state. The subsets were then merged to create three balanced datasets: Training, Validation, and Test, each with an equal number of frames for each state. Finally, the balanced datasets were shuffled again and resized to maintain the required split ratio of 70% for training, 15% for validation, and 15% for testing. The balanced dataset will be used for training and evaluating the object detection model, while the full dataset will be utilised for sequence model training and framework evaluation. The resulting distribution of frames across the train, test, and validation sets for each state after balancing is shown in Table 3.3.

Dataset	Total Frames
Train	3534 (69.57%)
Test	773 (15.22%)
Val	773 (15.22%)

Table 3.3: Distribution of frames across train, test, and validation sets for each state in the AARP dataset after balancing.

The primary reason for balancing the dataset is to ensure that the object detection model is equally trained on all states of the refuelling port. An imbalanced dataset could cause the model to perform well on the more common states (like CLOSED) while underperforming on the less common states (like OPEN and SEMI-OPEN). By balancing the dataset, the model has an equal opportunity to learn from all states, improving its generalisation and robustness.

3.1.6 Example Images from the Datase

Figure 3.2, Figure 3.3, and Figure 3.4 show annotated images of the refuelling port in the CLOSED, SEMI-OPEN, and OPEN states, respectively.

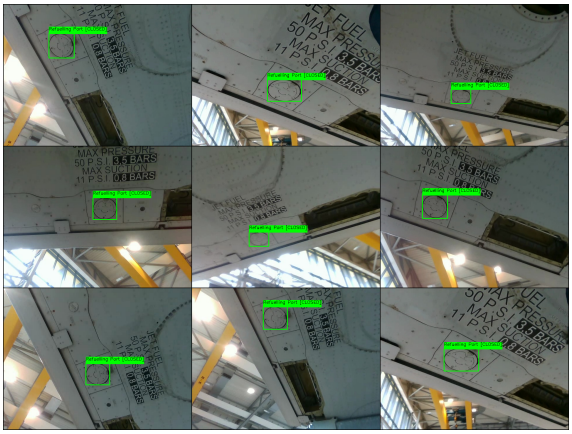

Figure 3.2: Annotated images of the refuelling port in the CLOSED state.

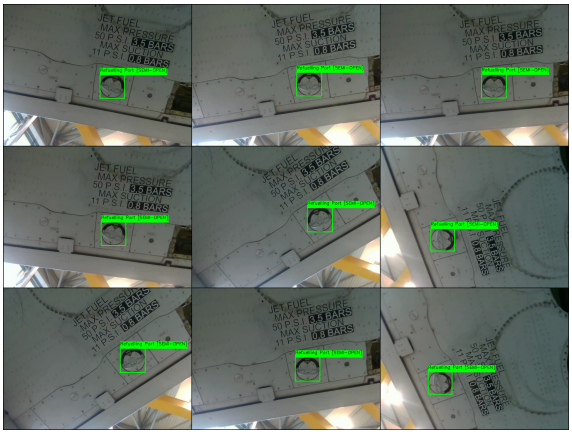

Figure 3.3: Annotated images of the refuelling port in the SEMI-OPEN state.

Figure 3.4: Annotated images of the refuelling port in the OPEN state.

3.1.7 Temporal Dynamics Analysis of the Refuelling Port

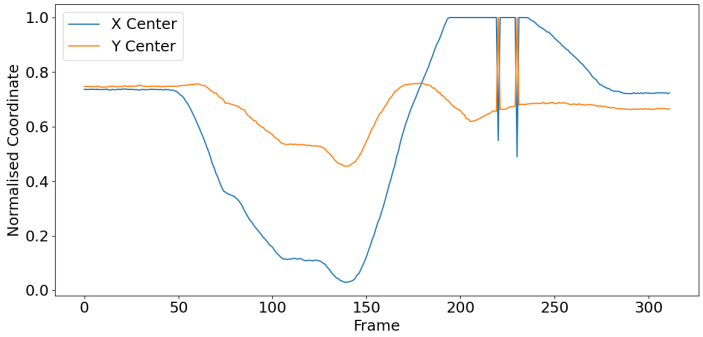

(a) Central Position over Time without Filter.

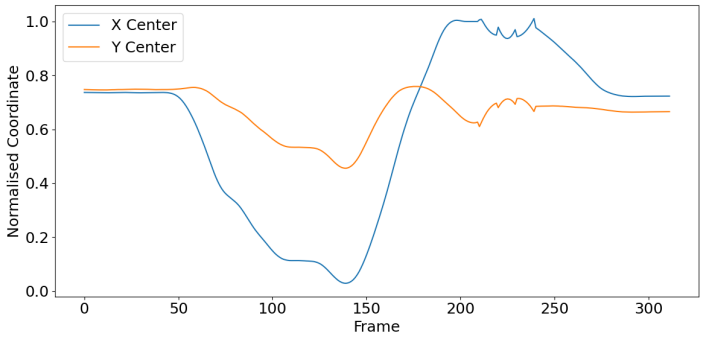

(b) Central Position over Time with Savitzky-Golay Filter.

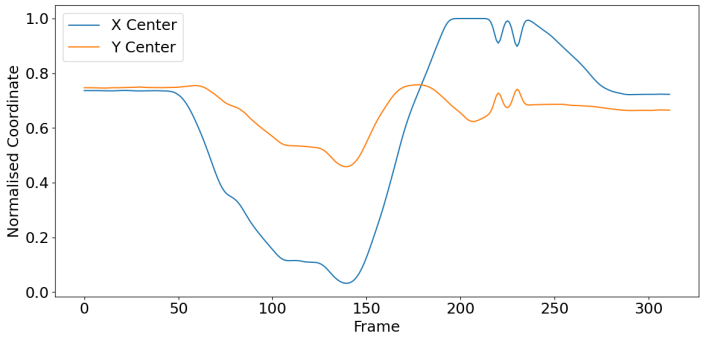

(c) Central Position over Time with Gaussian Filter.

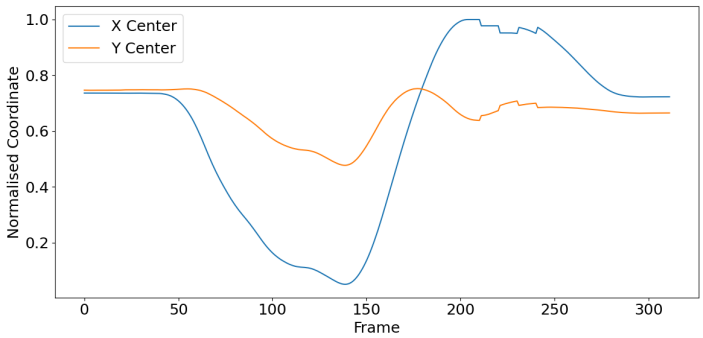

(d) Central Position over Time with Rolling Mean Filter.

Figure 3.5: Temporal analysis of refuelling port central position in video *test_indoor1*.

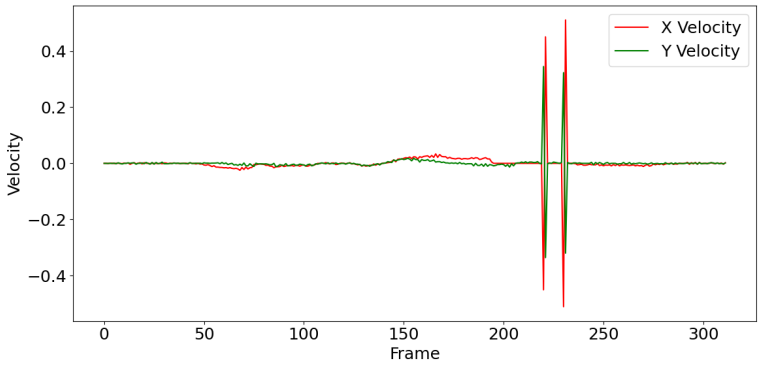

(a) Velocity over Time without Filter.

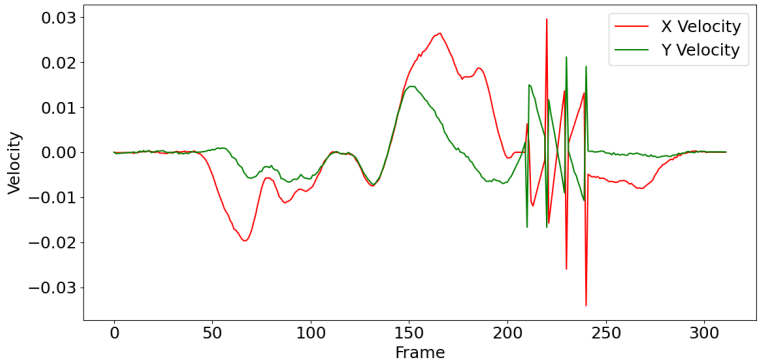

(b) Velocity over Time with Savitzky-Golay Filter.

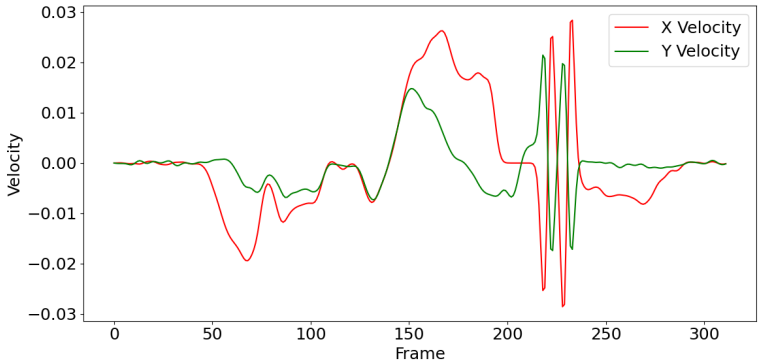

(c) Velocity over Time with Gaussian Filter.

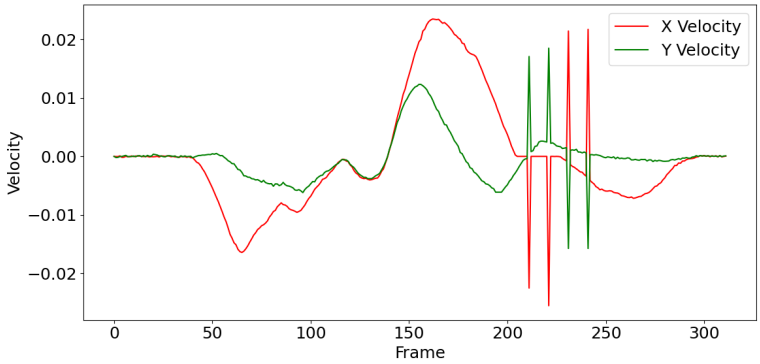

(d) Velocity over Time with Rolling Mean Filter.

Figure 3.6: Temporal analysis of refuelling port velocity in video *test_indoor1*.

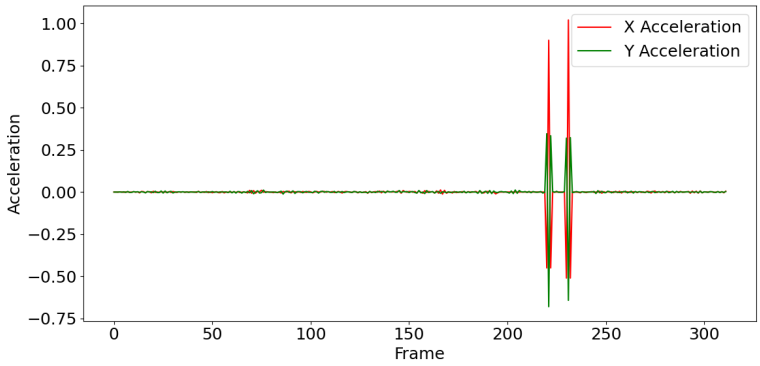

(a) Acceleration over Time without Filter.

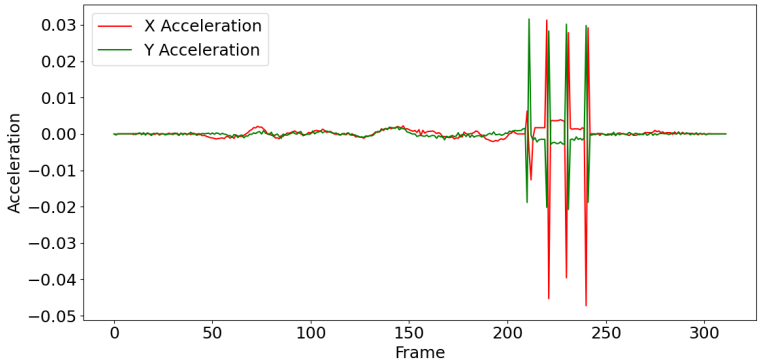

(b) Acceleration over Time with Savitzky-Golay Filter.

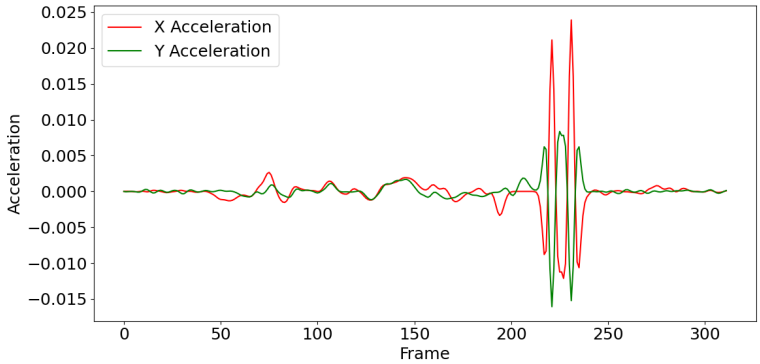

(c) Acceleration over Time with Gaussian Filter.

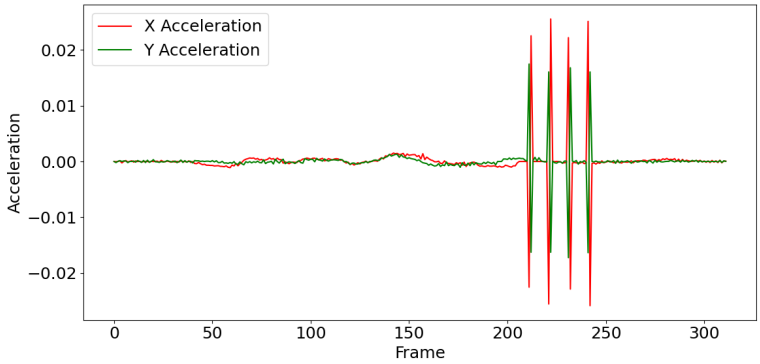

(d) Acceleration over Time with Rolling Mean Filter.

Figure 3.7: Temporal analysis of refuelling port acceleration in video *test_indoor1*.

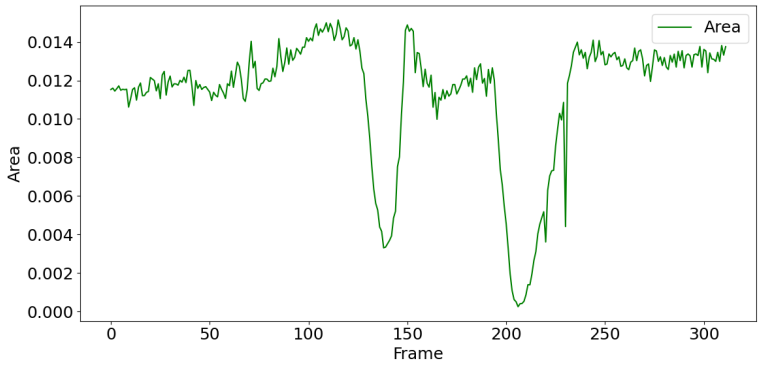

(a) Area over Time without Filter.

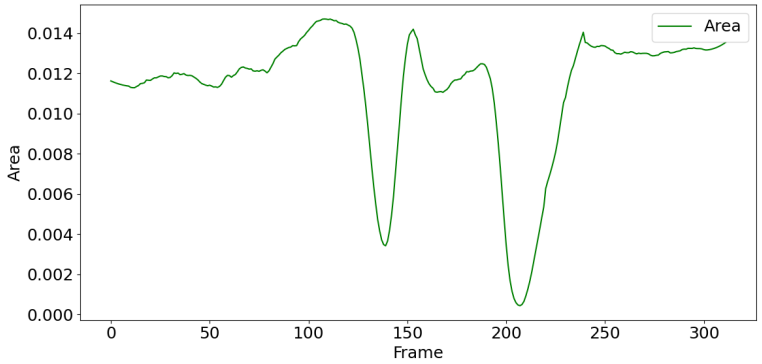

(b) Area over Time with Savitzky-Golay Filter.

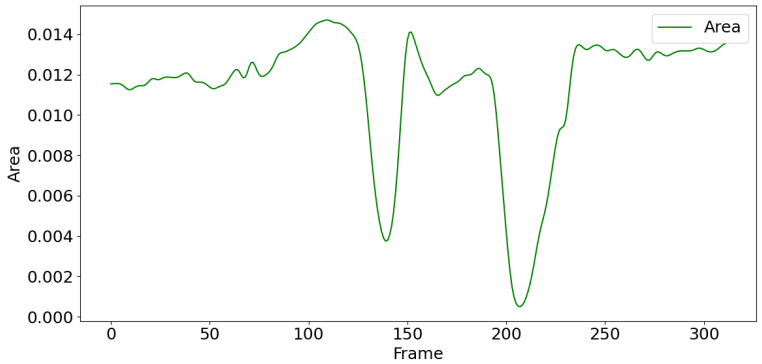

(c) Area over Time with Gaussian Filter.

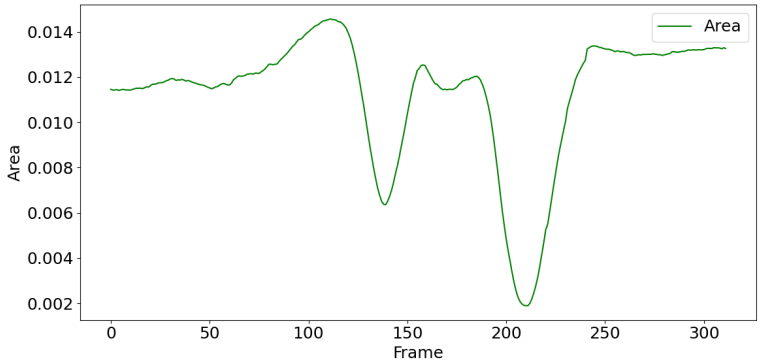

(d) Area over Time with Rolling Mean Filter.

Figure 3.8: Temporal analysis of refuelling port size in video *test_indoor1*.

In this analysis, different filters were applied to the refuelling port data to improve the clarity and reliability of the temporal dynamics, which are essential for training sequence models. The filters tested include the Savitzky-Golay filter, Gaussian filter, and Rolling Mean filter. Each of these filters has unique characteristics in how they reduce noise and preserve data trends, making them suitable for different analytical needs. The Savitzky-Golay filter smooths the data by applying a polynomial regression to a sliding window, effectively reducing high-frequency noise while preserving the shape and essential characteristics of the signal [59, 60]. This makes it ideal for situations where maintaining the integrity of the data trend is critical. The Gaussian filter, on the other hand, applies a Gaussian function to smooth the data, which helps in reducing noise by softening sharp edges and making the overall trend more observable, though at the cost of potentially blurring finer details [54]. The Rolling Mean filter computes a moving average over the data, which smooths out short-term fluctuations and emphasises longer-term trends, but this method can sometimes oversmooth the data, potentially obscuring subtle but important variations [63].

Firstly, the central position of the refuelling port was tracked over time to assess its movement along the X and Y axes, as shown in Figure 3.5. The raw data (Figure 3.5a) displayed substantial noise, particularly in the X coordinate, which made it challenging to discern the true movement of the refuelling port. Applying the Savitzky-Golay filter (Figure 3.5b) effectively smoothed out the noise while retaining the essential trend of the central position, allowing for the preservation of important variations in the data that might indicate significant movement patterns. In contrast, the Rolling Mean filter (Figure 3.5d) offered a similar level of smoothing but tended to oversmooth the data, potentially obscuring critical inflection points that are necessary for accurate predictions. The Gaussian filter (Figure 3.5c) also provided smoothing, but with a slight reduction in the preservation of smaller fluctuations, which could be significant for predictive tasks. Then, velocity was analysed by differentiating the central position over time, as depicted in Figure 3.6. The raw velocity data (Figure 3.6a) was noisy, with sharp spikes indicating erratic changes in speed that could be artifacts. The Savitzky-Golay filter (Figure 3.6b) smoothed these spikes, making the data more interpretable and highlighting consistent trends that would help the sequence model learn meaningful patterns. The Gaussian filter (Figure 3.6c) provided a similar smoothing effect, ensuring gradual and reflective changes in velocity. However, it slightly dampened the sharp transitions that might be relevant for identifying sudden movements. The Rolling Mean filter (Figure 3.6d) effectively reduced noise but risked removing crucial data about sudden movements necessary for accurate predictions. Acceleration, derived as the second derivative of the central position, was analysed in its raw form (Figure 3.7a) and through the application of filters (Figures 3.7b, 3.7c, and 3.7d). The raw acceleration data exhibited extreme spikes, which were effectively smoothed by the Savitzky-Golay filter, resulting in a clearer signal that still captured essential trends. The Gaussian filter also provided a comparable smoothing effect, but the Rolling Mean filter's tendency to oversmooth could obscure real changes in acceleration that are critical for the model to learn. Finally, the area of the refuelling port, representing its size over time, was analysed in Figure 3.8. The raw area data fluctuated considerably, with abrupt changes likely due to noise or occlusions in the video data (Figure 3.8a). Smoothing was necessary to understand the true size changes, with the Savitzky-Golay filter proving effective in reducing noise while preserving key trends, making the data more reliable for training the sequence model. The Gaussian filter also performed well, particularly in moderately noisy data, but the Rolling Mean filter's tendency to oversmooth suggests it may not be suitable when detailed temporal patterns are important.

In conclusion, the Savitzky-Golay filter consistently balanced noise reduction with the

preservation of critical temporal dynamics, making it the recommended preprocessing method for training a sequence model. The Gaussian filter also performed adequately, especially in scenarios where reducing noise is a priority, but it should be used with caution to avoid over-smoothing important data features. The Rolling Mean filter, while useful in certain contexts, often risked obscuring meaningful patterns, making it less suitable for applications requiring detailed temporal analysis. Therefore, the Savitzky-Golay filter will be used here for preparing the data to train the sequence model to predict the refuelling port's future positions and sizes.

3.2 Framework Design

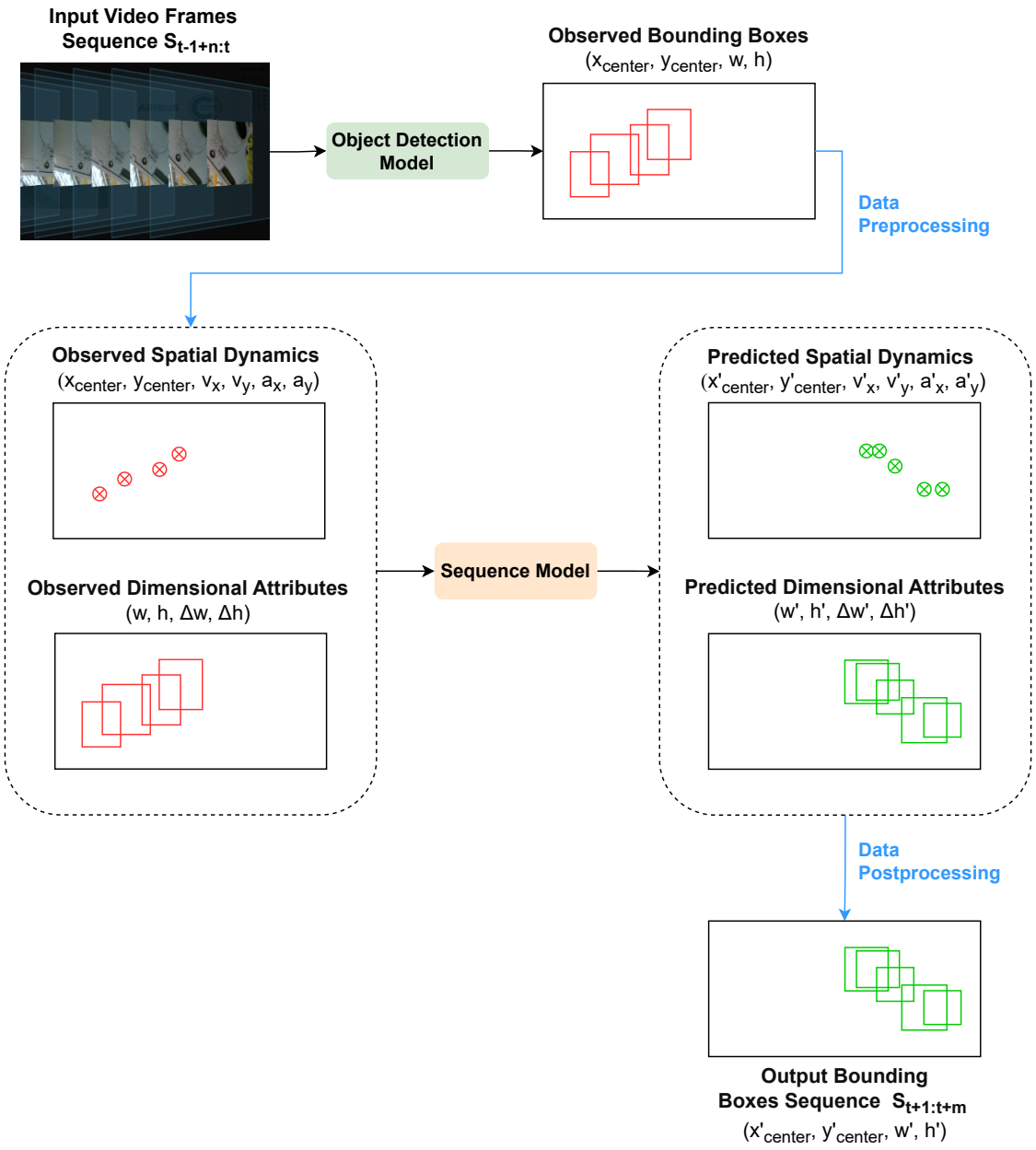

Figure 3.9: Framework Workflow

The proposed framework, illustrated in Figure 3.9, is designed to predict the future positions of the refuelling port's bounding boxes across the next m frames of a video stream. The objective is to forecast a sequence of future bounding boxes, $\mathbf{S}_{t+1:t+m} = \{\mathbf{b}_{t+1}, \ldots, \mathbf{b}_{t+m}\}$, based on the observed bounding boxes from the past n frames, $\mathbf{S}_{t-n+1:t} = \{\mathbf{b}_{t-n+1}, \ldots, \mathbf{b}_t\}$. The process begins with an input video sequence, which is analysed on a frame-by-frame basis. An object detection model first identifies and locates the bounding boxes of the refuelling port in each frame. At any given time step t, the observed bounding box is denoted as $\mathbf{b}_t = [x_t, y_t, w_t, h_t]$, where (x_t, y_t) represent the centre coordinates of the bounding box, and w_t and h_t represent the width and height of the bounding box, respectively. These detected bounding boxes are then formatted into input vectors suitable for the sequence model. The sequence model is responsible for predicting the future spatial positions and dimensions of the refuelling port's bounding boxes. Finally, these predictions are refined through post-processing steps to produce the final bounding box forecasts for the subsequent frames.

3.3 Object Detection Model Fine-tuning

A fine-tuned YOLOv10S model is used to detect the refuelling port within the video frames, as depicted in the object detection model section of Figure 3.9. As highlighted in the literature review, YOLOv10 represents the latest advancement in object detection technology, offering an optimal balance between speed and accuracy. The YOLOv10S variant is particularly well-suited for real-time applications, especially on resource-constrained embedded devices, due to its lightweight architecture. The model is fine-tuned through transfer learning on the AARP dataset, enabling precise detection of the refuelling port within the video frames. This fine-tuning process ensures that the model meets the demands of real-time video analysis with both accuracy and responsiveness. The implementation uses the Ultralytics YOLOv10 framework [35], which provides a reliable and efficient pipeline for both training and inference. This framework optimises detection performance and guarantees robust operation in different scenarios.

3.4 Sequence Model Design

This thesis introduces a novel deep learning sequence model, named *SizPos-GRU*, specifically designed for predicting the future positions and sizes of a unique object in a video stream. The *SizPos-GRU* model leverages an encoder-attention-decoder architecture to effectively capture both temporal dependencies and spatial relationships in the data. The *SizPos-GRU* framework consists of four main components: two encoders, an attention mechanism, and two decoders. Each component is meticulously designed to handle specific aspects of the sequence modelling task, from encoding input sequences to generating context-aware predictions. This custom architecture ensures accurate and efficient prediction of future object trajectories and dimensions within video streams.

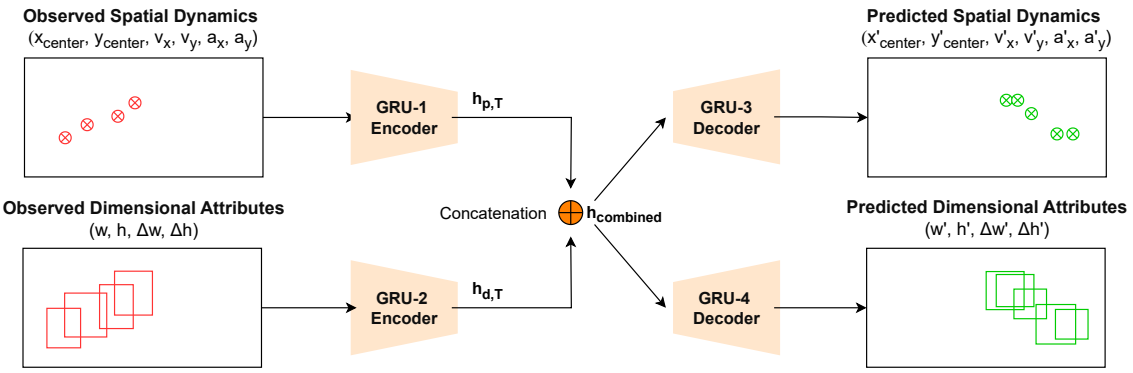

Figure 3.10: *SizPos-GRU* model Architecture

3.4.1 Input Representation

The *SizPos-GRU* model expects two types of input sequences to predict future positions and sizes of an object. The first input captures the spatial dynamics of the object, including its position, velocity, and acceleration. The second input focuses on the object's dimensional attributes, such as its width and height, and changes in these dimensions over time.

Spatial Dynamics Vector

The spatial dynamics vector at time t, denoted as $\mathbf{p}_t$, represents the position, velocity, and acceleration of the bounding box center. It is defined as follows:

$$\mathbf{p}_t = (x_t, y_t, v_{x,t}, v_{y,t}, a_{x,t}, a_{y,t}), \tag{3.1}$$

$$v_{x,t} = x_t - x_{t-1}, \quad v_{y,t} = y_t - y_{t-1}, \tag{3.2}$$

$$a_{x,t} = v_{x,t} - v_{x,t-1}, \quad a_{y,t} = v_{y,t} - v_{y,t-1}. \tag{3.3}$$

As shown in Equation (3.1), the spatial dynamics vector $\mathbf{p}_t$ includes the center coordinates (x_t, y_t), the velocities $(v_{x,t}, v_{y,t})$, and the accelerations $(a_{x,t}, a_{y,t})$. Equations (3.2) and (3.3) define the velocities and accelerations along the x and y axes, respectively.

Dimensional Attributes Vector

The dimensional attributes vector at time t, denoted as $\mathbf{d}_t$, captures the size of the bounding box and the changes in its dimensions:

$$\mathbf{d}_t = (w_t, h_t, \Delta w_t, \Delta h_t), \tag{3.4}$$

$$\Delta w_t = w_t - w_{t-1}, \quad \Delta h_t = h_t - h_{t-1}. \tag{3.5}$$

Equation (3.4) defines the dimensional attributes vector $\mathbf{d}_t$, which includes the width (w_t), height (h_t), and the changes in these dimensions, as defined by Δw_t and Δh_t in Equation (3.5).

Input Sequences for Model

The sequences of these vectors over a time window of n frames are fed into the model as:

$$\mathbf{P} = \{\mathbf{p}_{t-1+n}, \mathbf{p}_{t-n+2}, \ldots, \mathbf{p}_t\}, \quad \mathbf{D} = \{\mathbf{d}_{t-1+n}, \mathbf{d}_{t-n+2}, \ldots, \mathbf{d}_t\},$$

where **P** represents the sequence of spatial dynamics vectors, and **D** represents the sequence of dimensional attributes vectors, as shown in Equation (3.4.1). These sequences are processed by the model's encoders to extract temporal features, which are then used to predict future bounding box positions and sizes.

3.4.2 Encoders

The *SizPos-GRU* model employs two separate GRU encoders: one for processing the sequence of spatial dynamics vectors and another for processing the sequence of dimensional attributes vectors. Both encoders are designed to extract meaningful temporal features from their respective input sequences, which are subsequently used by the decoders to generate predictions. In Figure 3.11, the input sequence $\mathbf{X} = \{\mathbf{x}_1, \mathbf{x}_2, \ldots, \mathbf{x}_T\}$ represents either the spatial dynamics vector (**P**) or the dimensional attributes vector (**D**). This sequence is processed through multiple GRU layers, producing a sequence of hidden states $H = \{h_1, h_2, \ldots, h_T\}$ and a final hidden state h_T that encapsulates the temporal dependencies in the input sequence.

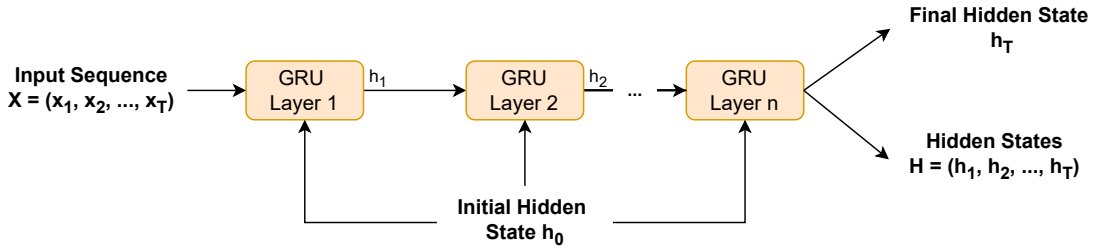

Figure 3.11: *SizPos-GRU* Encoder Architecture.

Position Encoder

The position encoder processes the sequence of spatial dynamics vectors, which include the bounding box's position, velocity, and acceleration over time. It is defined as:

$$H_p, h_{pT} = \text{GRU}_p(\mathbf{P}, h_{p0}), \tag{3.6}$$

Equation (3.6) describes the position encoder, where H_p is the sequence of hidden states generated by the GRU, and h_{pT} is the final hidden state at time T.

Size Encoder

The size encoder processes the sequence of dimensional attributes vectors, which include the bounding box's width, height, and changes in these dimensions over time. It is defined as:

$$H_d, h_{dT} = \text{GRU}_d(\mathbf{D}, h_{d0}), \tag{3.7}$$

Equation (3.7) outlines the size encoder, where H_d represents the sequence of hidden states generated by the GRU, and h_{dT} is the final hidden state at time T.

3.4.3 Hidden State Fusion

After the position and size encoders process their respective input sequences, the resulting hidden states are combined to leverage information from both spatial dynamics and dimensional attributes. This fusion is achieved by concatenating the final hidden states from both encoders and passing them through a fully connected layer:

$$h_{\text{combined}} = W_{\text{combine}} \cdot [h_{p_T} \oplus h_{d_T}] + b_{\text{combine}}, \tag{3.8}$$

As shown in Equation (3.8), the final hidden states from the position and size encoders are concatenated and passed through a fully connected layer to produce the fused hidden state h_{combined}. This fused state encapsulates the temporal features from both input sequences, enabling the model to generate context-aware predictions.

3.4.4 Decoders

The *SizPos-GRU* model utilises two specialised decoders to predict the future bounding boxes over the next m frames. These decoders are designed to process the temporal features extracted by the encoders and the fused hidden states, generating accurate and context-aware predictions. Figure 3.12 illustrates the decoding process where the input sequence $\mathbf{x}_t$ and the last hidden state h_{t-1} are processed through multiple GRU layers to generate the next hidden state h_t. The sequence of hidden states $H = \{h_1, h_2, \ldots, h_t\}$ is then passed through a self-attention mechanism, which calculates attention scores and weights. The weighted sum of hidden states is combined with linear and non-linear transformations, including dropout and ReLU activation functions, to produce the final output $\mathbf{x}_{t+1}$. This output is used for predicting the next time step in the sequence, continuing the process iteratively for future predictions.

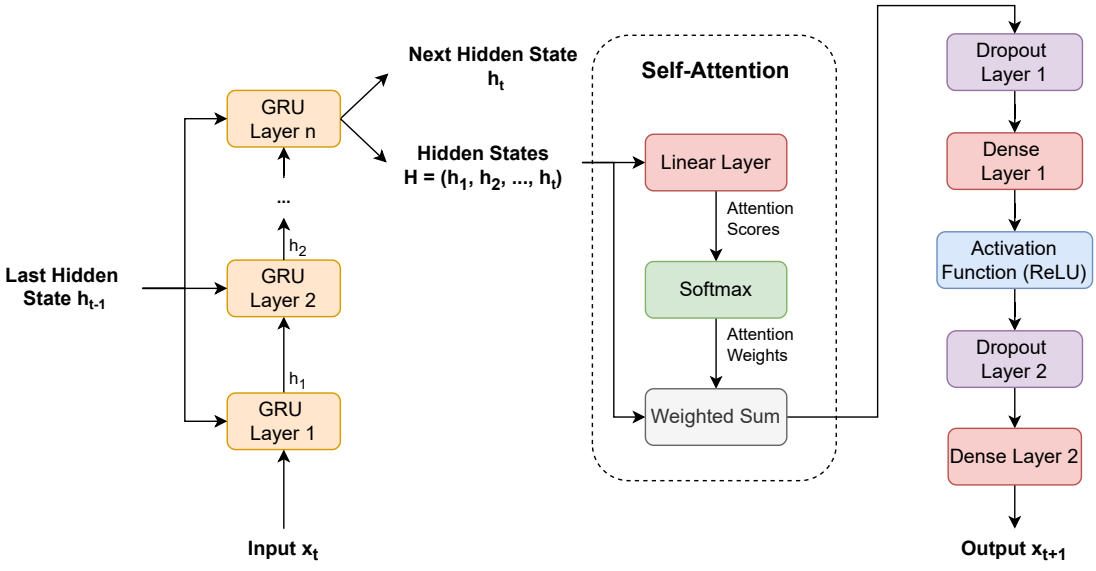

Figure 3.12: *SizPos-GRU* Decoder Architecture.

Position Decoder

The position decoder is responsible for predicting the future spatial dynamics of the bounding boxes, including their positions and velocities. The decoding process begins by initialising the

input with the last observed position in the sequence. The decoder then iteratively predicts future positions over the defined prediction horizon m. During each iteration, the current input is processed through a stack of GRU layers, which update the hidden state based on the previous hidden state and current input. This updated hidden state, encapsulating temporal dependencies, is then passed through a self-attention mechanism. The self-attention mechanism computes attention scores, which are normalised using a softmax function to produce attention weights. These weights are applied to the hidden states to generate a context vector that highlights the most relevant temporal features. The GRU layers within the position decoder generate the sequence of hidden states H_p as shown in Equation (3.9), where H_p is derived from processing the combined hidden states. The attention scores α_i are calculated using a linear transformation of each hidden state h_{p_i} (Equation (3.10)), and these scores are normalised to produce the attention weights. The context vector c_p is then computed as the weighted sum of the hidden states, as defined in Equation (3.11).

$$H_p = \text{GRU}_p(h_{\text{combined}}), \tag{3.9}$$

$$\alpha_i = \frac{\exp(w_i)}{\sum_{j=1}^{m} \exp(w_j)}, \quad w_i = \text{Linear}(h_{p_i}), \tag{3.10}$$

$$c_p = \sum_{i=1}^{m} \alpha_i h_{p_i}, \tag{3.11}$$

The context vector c_p is then passed through a series of fully connected layers, with dropout and ReLU activation functions, to produce the final position prediction for the current time step. The process is defined by Equation (3.12), where the context vector is transformed and refined through the network to generate the output prediction:

$$\hat{\mathbf{P}}_{t+1:m} = \text{ReLU}(\text{Dropout}(\text{Dense1}(c_p))), \tag{3.12}$$

$$\hat{\mathbf{P}}_{t+1:m} = \text{Dense2}(\hat{\mathbf{P}}_{t+1:m}), \tag{3.13}$$

As defined in Equation (3.13), the predicted position $\hat{\mathbf{P}}_{t+1:m}$ is then used as the input for the next iteration of the decoding loop, enabling the model to recursively generate predictions for subsequent time steps. This iterative process continues until predictions for all future time steps within the prediction window have been generated, and the accumulated sequence of predicted positions is returned as the final output.

Size Decoder

The size decoder operates similarly to the position decoder but focuses on predicting the future dimensions of the bounding boxes, such as width and height. The decoding process starts with the last observed size in the sequence, and the decoder iteratively generates predictions for future sizes over the prediction horizon m. In each iteration, the current size input is processed through GRU layers that capture the temporal dynamics of size changes. The output from the GRU is then passed through a self-attention mechanism, which assigns different weights to the hidden states across time. These weights are used to compute a context vector c_d, which represents the most relevant temporal and spatial information for the current prediction step. The GRU layers within the size decoder generate the sequence of hidden states H_d as shown in Equation (3.14), where H_d is derived from processing the combined hidden states. The attention scores β_i are calculated using a linear transformation of each hidden state h_{d_i} (Equation (3.15)),

and these scores are normalised to produce the attention weights. The context vector c_d is then computed as the weighted sum of the hidden states, as defined in Equation (3.16).

$$H_d = \text{GRU}_d(h_{\text{combined}}), \tag{3.14}$$

$$\beta_i = \frac{\exp(v_i)}{\sum_{j=1}^{m} \exp(v_j)}, \quad v_i = \text{Linear}(h_{d_i}), \tag{3.15}$$

$$c_d = \sum_{i=1}^{m} \beta_i h_{d_i}, \tag{3.16}$$

The context vector c_d is passed through dense layers with dropout and ReLU activation to produce the final size prediction as shown in Equation (3.17). The process refines the context vector through transformations to generate the output prediction:

$$\hat{\mathbf{D}}_{t+1:m} = \text{ReLU}(\text{Dropout}(\text{Dense1}(c_d))), \tag{3.17}$$

$$\hat{\mathbf{D}}_{t+1:m} = \text{Dense2}(\hat{\mathbf{D}}_{t+1:m}), \tag{3.18}$$

Similar to the position decoder, the predicted size $\hat{\mathbf{D}}_{t+1:m}$ (Equation (3.18)) is then used as input for the next iteration, ensuring that each prediction is contextually informed by previous outputs. This loop continues until the decoder has generated predictions for all future time steps within the prediction window m, which are then returned as the sequence of predicted sizes.

3.5 Algorithm Design

3.5.1 Calculation of Key Values for Loss Functions

In the *SizPos-GRU* model, several values are calculated to derive the loss functions that guide the model training and optimisation process. These values are obtained by transforming the model's raw outputs into meaningful metrics that can be compared with the ground truth data. The key values calculated include:

Bounding Box and Velocity Estimation

For each time step t, the model predicts spatial dynamics $\hat{\mathbf{p}}_t$ and dimensional attributes $\hat{\mathbf{d}}_t$. These predictions are used to estimate bounding boxes and velocities, as shown in Equations (3.19) to (3.26):

$$\hat{b}_{x,t} = \hat{p}_{x,t}, \tag{3.19}$$

$$\hat{b}_{y,t} = \hat{p}_{y,t}, \tag{3.20}$$

$$\hat{b}_{w,t} = \hat{d}_{w,t}, \tag{3.21}$$

$$\hat{b}_{h,t} = \hat{d}_{h,t}, \tag{3.22}$$

$$\hat{v}_{x,t} = \hat{p}_{x,t} - \hat{p}_{x,t-1}, \tag{3.23}$$

$$\hat{v}_{y,t} = \hat{p}_{y,t} - \hat{p}_{y,t-1}, \tag{3.24}$$

$$\hat{v}_{w,t} = \hat{d}_{w,t} - \hat{d}_{w,t-1}, \tag{3.25}$$

$$\hat{v}_{h,t} = \hat{d}_{h,t} - \hat{d}_{h,t-1}. \tag{3.26}$$

Here, $\hat{b}_{x,t}, \hat{b}_{y,t}, \hat{b}_{w,t}, \hat{b}_{h,t}$ represent the predicted bounding box's center coordinates, width, and height at time t, and $\hat{v}_{x,t}, \hat{v}_{y,t}, \hat{v}_{w,t}, \hat{v}_{h,t}$ represent the corresponding velocities.

Velocity to Position Conversion

To derive future positions from the predicted velocities, the following equations are used:

$$\hat{p}_{x,t+1} = \hat{p}_{x,t} + \hat{v}_{x,t}, \tag{3.27}$$
$$\hat{p}_{y,t+1} = \hat{p}_{y,t} + \hat{v}_{y,t}, \tag{3.28}$$
$$\hat{d}_{w,t+1} = \hat{d}_{w,t} + \hat{v}_{w,t}, \tag{3.29}$$
$$\hat{d}_{h,t+1} = \hat{d}_{h,t} + \hat{v}_{h,t}. \tag{3.30}$$

As indicated in Equations (3.27) to (3.30), these equations are used iteratively to predict the positions and sizes at each future time step, integrating the model's output over time.

3.5.2 Loss Function Formulation

To train the *SizPos-GRU* model, Smooth L1 Loss, also known as Huber Loss, a composite loss function is employed, which takes into account various aspects of prediction accuracy. This loss function is a combination of L1 and L2 losses, providing a balance between the two, making it less sensitive to outliers than L2 loss while avoiding the large gradient changes associated with L1 loss. The loss functions have been applied to various aspects of the model predictions:

Size and Position Loss

The model calculates the Smooth L1 Loss for the predicted sizes and positions compared to the ground truth data:

$$\mathscr{L}_{\text{size}} = \frac{1}{N} \sum_{t=1}^{m} \sum_{i \in \{w,h\}} \text{SmoothL1}\left(\hat{d}_{i,t}, d_{i,t}^{gt}\right), \tag{3.31}$$

$$\mathscr{L}_{\text{position}} = \frac{1}{N} \sum_{t=1}^{m} \sum_{i \in \{x,y\}} \text{SmoothL1}\left(\hat{p}_{i,t}, p_{i,t}^{gt}\right). \tag{3.32}$$

Here, $\mathscr{L}_{\text{size}}$ and $\mathscr{L}_{\text{position}}$ are the size and position loss functions, respectively, as shown in Equations (3.31) and (3.32), where $\text{SmoothL1}(a,b)$ is defined as:

$$\text{SmoothL1}(a,b) = \begin{cases} 0.5 \times (a-b)^2 & \text{if } |a-b| < 1 \\ |a-b| - 0.5 & \text{otherwise.} \end{cases} \tag{3.33}$$

Equation (3.33) defines the Smooth L1 function, which balances L1 and L2 loss characteristics to manage prediction errors.

Bounding Box Loss

The model also computes the loss for the predicted bounding boxes, which represent the object's position and size in a unified format. The bounding box at each time step t is given by $\hat{\mathbf{b}}_t = (\hat{b}_{x,t}, \hat{b}_{y,t}, \hat{b}_{w,t}, \hat{b}_{h,t})$. The loss for these predictions is calculated as:

$$\mathscr{L}_{\text{bbox}} = \frac{1}{N} \sum_{t=1}^{m} \sum_{i \in \{x,y,w,h\}} \text{SmoothL1} \left(\hat{b}_{i,t}, b_{i,t}^{gt} \right), \tag{3.34}$$

where $b_{i,t}^{gt}$ represents the ground truth bounding box coordinates and dimensions at time t, as shown in Equation (3.34).

Velocity-to-Position Loss

To ensure that the predicted velocities accurately translate to future positions, the model includes a loss term that compares the predicted positions derived from velocities ($\hat{p}_{x,t+1}$, $\hat{p}_{y,t+1}$, $\hat{d}_{w,t+1}$, $\hat{d}_{h,t+1}$) with the ground truth positions and sizes at the next time step:

$$\mathscr{L}_{\text{vel-to-pos}} = \frac{1}{N} \sum_{t=1}^{m} \sum_{i \in \{x,y,w,h\}} \text{SmoothL1} \left(\hat{p}_{i,t+1}, p_{i,t+1}^{gt} \right). \tag{3.35}$$

As defined in Equation (3.35), this loss term ensures that the model's predicted velocities are consistent with the subsequent positions, reinforcing the temporal coherence of the predictions.

Total Loss

The total loss used for model training is the sum of all the individual losses:

$$\mathscr{L}_{\text{total}} = \mathscr{L}_{\text{size}} + \mathscr{L}_{\text{position}} + \mathscr{L}_{\text{bbox}} + \mathscr{L}_{\text{vel-to-pos}}. \tag{3.36}$$

Equation (3.36) defines the total loss function $\mathscr{L}_{\text{total}}$, which aggregates all loss components to guide the training and optimisation process of the *SizPos-GRU* model.

3.5.3 Data Postprocessing

Post-processing is a crucial step in the proposed prediction pipeline that refines the raw predictions generated by the model. The main objective is to enhance the accuracy and smoothness of the predicted bounding box trajectories of the aircraft refuelling port. Several smoothing techniques are applied to reduce noise and eliminate unrealistic variations in the predicted trajectories. These techniques ensure that the final output is both accurate and visually coherent.

Savitzky-Golay Filter

The Savitzky-Golay filter is a digital filter used to smooth data while preserving its shape and features. It works by fitting successive subsets of data points with a low-degree polynomial. The filter is particularly effective in reducing noise without significantly distorting the signal. Given a trajectory $\mathbf{y} = \{y_1, y_2, \ldots, y_n\}$, the smoothed value at point i is obtained by fitting a polynomial of degree k over a window of size $2m+1$ centered at i:

$$\hat{y}_i = \sum_{j=-m}^{m} c_j y_{i+j}, \tag{3.37}$$

where c_j are the coefficients determined by the polynomial fit, as shown in Equation (3.37).

Moving Average Smoothing

Moving average smoothing is a simple technique that calculates the average of a sliding window of data points, effectively reducing short-term fluctuations and highlighting longer-term trends. For a given trajectory $\mathbf{y}$, the smoothed value at point i using a window of size w is computed as:

$$\hat{y}_i = \frac{1}{w} \sum_{j=0}^{w-1} y_{i-j}, \tag{3.38}$$

as indicated in Equation (3.38). This method is straightforward and helps to smooth out irregularities in the trajectory.

Exponential Smoothing

Exponential smoothing assigns exponentially decreasing weights to past observations, making it suitable for time-series data where recent data points are more relevant. The smoothed value at time t is given by:

$$\hat{y}_t = \alpha y_t + (1-\alpha)\hat{y}_{t-1}, \tag{3.39}$$

where α is the smoothing factor, $0 < \alpha \leq 1$, and $\hat{y}_{t-1}$ is the previously smoothed value, as shown in Equation (3.39).

Adaptive Smoothing

Adaptive smoothing adjusts the degree of smoothing based on the variation observed in the data. If a significant change is detected between consecutive data points, more aggressive smoothing is applied. Given a trajectory $\mathbf{y}$, the adaptive smoothing is defined as:

$$\hat{y}_t = \begin{cases} \text{Smooth}(\mathbf{y}_{t-k:t}) & \text{if } |y_t - y_{t-1}| > \text{threshold}, \\ y_t & \text{otherwise}, \end{cases} \tag{3.40}$$

where $\text{Smooth}(\mathbf{y}_{t-k:t})$ applies a smoothing filter over the recent k data points, as described in Equation (3.40).

Hybrid Smoothing

Hybrid smoothing combines multiple smoothing techniques to leverage their strengths. Typically, a Savitzky-Golay filter is applied first, followed by a moving average smoothing on the already smoothed trajectory. Let $\hat{\mathbf{y}}^{(1)}$ be the output of the Savitzky-Golay filter applied to $\mathbf{y}$. The final smoothed trajectory $\hat{\mathbf{y}}^{(2)}$ is obtained by applying a moving average:

$$\hat{\mathbf{y}}^{(2)} = \frac{1}{w} \sum_{j=0}^{w-1} \hat{y}^{(1)}_{i-j}, \tag{3.41}$$

where w is the window size for the moving average, as indicated in Equation (3.41).

Kalman Filter Smoothing

The Kalman Filter is a statistical method used to estimate the state of a dynamic system from a series of noisy measurements. In our context, it is used to smooth the predicted bounding box trajectories by estimating the underlying motion parameters. The Kalman Filter operates in two main steps: prediction and update. The predicted state $\mathbf{x}_{t|t-1}$ and its covariance $\mathbf{P}_{t|t-1}$ are computed as:

$$\mathbf{x}_{t|t-1} = \mathbf{F}\mathbf{x}_{t-1|t-1}, \tag{3.42}$$

$$\mathbf{P}_{t|t-1} = \mathbf{F}\mathbf{P}_{t-1|t-1}\mathbf{F}^T + \mathbf{Q}, \tag{3.43}$$

where $\mathbf{F}$ is the state transition matrix, and $\mathbf{Q}$ is the process noise covariance matrix, as shown in Equations (3.42) and (3.43). The update step corrects the prediction using the actual measurement $\mathbf{z}_t$:

$$\mathbf{K}_t = \mathbf{P}_{t|t-1}\mathbf{H}^T(\mathbf{H}\mathbf{P}_{t|t-1}\mathbf{H}^T + \mathbf{R})^{-1}, \tag{3.44}$$

$$\mathbf{x}_{t|t} = \mathbf{x}_{t|t-1} + \mathbf{K}_t(\mathbf{z}_t - \mathbf{H}\mathbf{x}_{t|t-1}), \tag{3.45}$$

$$\mathbf{P}_{t|t} = (\mathbf{I} - \mathbf{K}_t\mathbf{H})\mathbf{P}_{t|t-1}, \tag{3.46}$$

where $\mathbf{K}_t$ is the Kalman gain, $\mathbf{H}$ is the measurement matrix, and $\mathbf{R}$ is the measurement noise covariance, as defined in Equations (3.44) to (3.46).

Chapter 4

Experiment Design

4.1 Experiment Environment

The experiments were conducted using a high-performance computing environment optimised for deep learning tasks. The hardware configuration included an NVIDIA A40 GPU with 48 GB of VRAM, 9 virtual CPUs (vCPUs), and 50 GB of RAM, ensuring efficient handling of large-scale models and data processing tasks. The software environment was based on a Linux operating system, utilising PyTorch Lightning [23] for sequence model implementation. PyTorch Lightning provided a streamlined and modular framework, improving experimentation and reproducibility. Data loading was managed using PyTorch's `DataLoader` [3] with 8 worker threads to maximise I/O efficiency.

4.2 Evaluation Metrics

In order to assess the performance of the proposed framework for predicting the future position of aircraft refuelling ports, it is imperative to utilise appropriate evaluation metrics that reflect both the accuracy and reliability of the predictions. This section outlines and discusses the four primary evaluation metrics employed in this study: Average Displacement Error (ADE), Final Displacement Error (FDE), Average Intersection over Union (AIoU), and Final Intersection over Union (FIoU). These metrics provide a comprehensive evaluation by measuring different aspects of the predicted trajectories and bounding boxes.

Average Displacement Error (ADE)

The Average Displacement Error (ADE) measures the average Euclidean distance between the predicted bounding box centers and the ground truth bounding box centers over all predicted frames. The ADE provides an overall measure of the spatial accuracy of the prediction model over time. It captures how closely the predicted trajectory follows the actual trajectory of the refuelling port. In practical terms, a lower ADE indicates that the model consistently predicts the position of the refuelling port with minimal deviation from its true path, which is critical in applications where continuous tracking and precise positioning are essential. It is defined as:

$$\text{ADE} = \frac{1}{m} \sum_{t=1}^{m} \sqrt{(x_t^{\text{pred}} - x_t^{\text{gt}})^2 + (y_t^{\text{pred}} - y_t^{\text{gt}})^2}, \tag{4.1}$$

where m is the number of predicted frames, $(x_t^{\text{pred}}, y_t^{\text{pred}})$ represents the center of the predicted bounding box at the t-th frame, and $(x_t^{\text{gt}}, y_t^{\text{gt}})$ represents the center of the ground truth bounding box at the same frame. Equation (4.1) shows that x_t^{pred}, y_t^{pred}, x_t^{gt}, y_t^{gt}, and *ADE* are expressed in pixels.

Final Displacement Error (FDE)

The Final Displacement Error (FDE) focuses on the accuracy of the predicted bounding box center in the final frame of the prediction horizon. The FDE is crucial for evaluating the model's performance at the end of the prediction sequence. It focuses on the model's ability to accurately predict the final position of the refuelling port. A lower FDE indicates a high level of precision in predicting the final position. It is defined as the Euclidean distance between the predicted and ground truth bounding box centers at the final frame T:

$$\text{FDE} = \sqrt{(x_T^{\text{pred}} - x_T^{\text{gt}})^2 + (y_T^{\text{pred}} - y_T^{\text{gt}})^2}. \tag{4.2}$$

As shown in Equation (4.2), $(x_T^{\text{pred}}, y_T^{\text{pred}})$ represents the center of the predicted bounding box at the final frame, and $(x_T^{\text{gt}}, y_T^{\text{gt}})$ represents the center of the ground truth bounding box at the same frame.

Average Intersection over Union (AIoU)

The Average Intersection over Union (AIoU) evaluates the overlap between the predicted bounding boxes and the ground truth bounding boxes, averaged over all predicted frames. AIoU provides an integrated measure of both the spatial accuracy and the dimensional consistency of the predicted bounding boxes over time. A higher AIoU indicates that the predicted bounding boxes consistently maintain a high degree of overlap with the ground truth, reflecting the model's ability to accurately track both the position and the scale of the refuelling port. This metric is particularly relevant in tasks where the object's size and shape are critical, as it ensures that the detected object not only matches the position but also the correct dimensions, which is vital for the subsequent physical interaction with the object. It is computed as:

$$\text{AIoU} = \frac{1}{m} \sum_{t=1}^{m} \frac{A(\mathbf{b}_t^{\text{pred}} \cap \mathbf{b}_t^{\text{gt}})}{A(\mathbf{b}_t^{\text{pred}} \cup \mathbf{b}_t^{\text{gt}})}, \tag{4.3}$$

where $A(\mathbf{b}_t^{\text{pred}} \cap \mathbf{b}_t^{\text{gt}})$ denotes the area of the intersection between the predicted bounding box $\mathbf{b}_t^{\text{pred}}$ and the ground truth bounding box $\mathbf{b}_t^{\text{gt}}$ at the t-th frame, and $A(\mathbf{b}_t^{\text{pred}} \cup \mathbf{b}_t^{\text{gt}})$ denotes the area of their union, as defined in Equation (4.3).

Final Intersection over Union (FIoU)

The Final Intersection over Union (FIoU) assesses the overlap between the predicted bounding box and the ground truth bounding box at the final frame of the prediction horizon. FIoU is a critical metric when the final prediction accuracy is more important than the performance across all frames. It measures how well the predicted bounding box fits the ground truth at the crucial final moment, which is important for tasks that rely on the precise final positioning of an object. For instance, in automated systems that involve docking or alignment tasks, ensuring that the final predicted bounding box is highly accurate in terms of both position and size is essential for

successful operation. A higher FIoU score implies a more reliable and accurate final prediction, which is indispensable in high-stakes applications where precision is paramount. It is defined as:

$$\text{FIoU} = \frac{A(\mathbf{b}_T^{\text{pred}} \cap \mathbf{b}_T^{\text{gt}})}{A(\mathbf{b}_T^{\text{pred}} \cup \mathbf{b}_T^{\text{gt}})}, \tag{4.4}$$

where $A(\mathbf{b}_T^{\text{pred}} \cap \mathbf{b}_T^{\text{gt}})$ and $A(\mathbf{b}_T^{\text{pred}} \cup \mathbf{b}_T^{\text{gt}})$ denote the intersection and union areas at the final frame m, respectively, as shown in Equation (4.4).

4.3 Model Training and Optimisation

Model Parameters

The *SizPos-GRU* model was trained using the Adam optimizer, which is known for its ability to adapt learning rates for each parameter, enhancing the convergence speed and stability of the training process [40, 39, 10]. Adam computes adaptive learning rates for each parameter by keeping track of both the first and second moments of the gradients. This optimizer was selected due to its proven efficiency in handling non-stationary objectives and noisy gradients, which are common in deep learning models. The learning rate was dynamically adjusted using a *ReduceLROnPlateau* scheduler. This scheduler is particularly effective in preventing the model from getting stuck in local minima by reducing the learning rate when the validation loss stops improving [39, 10]. The learning rate LR_{new} is updated according to the following rule:

$$\text{LR}_{\text{new}} = \text{LR}_{\text{current}} \times \text{scheduler\_factor}, \tag{4.5}$$

where scheduler_factor is a predefined factor, typically set to a value less than 1, which controls how significantly the learning rate is reduced, as shown in Equation (4.5). This approach allows the model to make finer updates as it converges, thereby improving the chances of finding a better local minimum. The training was conducted with close monitoring of validation performance to ensure the model's ability to generalize to unseen data. By using early stopping based on validation metrics, the training process was made more efficient, preventing overfitting and ensuring that the model retained its ability to perform well on new data. Tables 4.1 and 4.2 provide an overview of the training configuration parameters used for the *SizPos-GRU* model. These parameters were selected based on the optimal results obtained from extensive hyperparameter tuning.

Table 4.1: Training Configuration Parameters for the *SizPos-GRU* model - Descriptions.

Parameter	**Description**
Random Seed	Seed value for reproducibility
Number of Workers	Number of CPU cores used for data loading
Batch Size	Number of samples per batch during training
Input Frames	Number of input frames fed into the model
Output Frames	Number of frames predicted by the model
Hidden Layer Size	Size of the hidden layers in the GRU network
Number of Layers	Number of GRU layers stacked in the network
Learning Rate	Initial learning rate for the optimizer
Scheduler Patience	Number of epochs to wait before reducing the learning rate
Scheduler Factor	Factor by which the learning rate is reduced
Max Epochs	Maximum number of epochs for training
Dropout Rate	Probability of dropping a neuron during training
Optimizer	Optimisation algorithm used for training
Scheduler	Learning rate scheduler used for dynamic adjustment
Checkpoint Metric	Metric used to save the best model checkpoint

Table 4.2: Training Configuration Parameters for the *SizPos-GRU* model - Values.

Parameter	**1 sec Prediction (30 frames)**	**2 sec Prediction (60 frames)**
Random Seed	42	42
Number of Workers	8	8
Batch Size	64	64
Input Frames	15	30
Output Frames	30	60
Hidden Layer Size	256	128
Number of Layers	8	8
Learning Rate	5×10^{-4}	5×10^{-4}
Scheduler Patience	10 epochs	10 epochs
Scheduler Factor	0.9	0.9
Max Epochs	100	100
Dropout Rate	0.2	0.2
Optimizer	Adam	Adam
Scheduler	ReduceLROnPlateau	ReduceLROnPlateau
Checkpoint Metric	Best Final FDE	Best Final FDE

Hyperparameter Tuning

Extensive hyperparameter tuning was conducted to determine the most effective configurations for the *SizPos-GRU* model. This process involved systematically varying key parameters to assess their impact on model performance. The goal was to strike a balance between model complexity and computational efficiency while ensuring that the model could learn effectively from the available data. Tables 4.3 and 4.4 summarise the hyperparameter tuning configuration, listing the range of values tested for each parameter. The tuning process included exploring different sizes and numbers of hidden layers, varying the number of input and output frames, and adjusting the learning rate, among other factors.

Table 4.3: Hyperparameter Tuning Configuration - Descriptions

Parameter	**Description**
Input Frames	Number of input frames fed into the model
Output Frames	Number of frames predicted by the model
Hidden Layer Sizes	Size of the hidden layers in the GRU network
Number of Hidden Layers	Number of GRU layers stacked in the network

Table 4.4: Hyperparameter Tuning Configuration - Values Tested

Parameter	**Values Tested**
Input Frames	15, 30
Output Frames	30, 60
Hidden Layer Sizes	32, 64, 128, 256, 512
Number of Hidden Layers	1, 2, 4, 8

The final selection of hyperparameters, informed by the tuning results, was critical in ensuring the *SizPos-GRU* model's effectiveness. The chosen parameters provided a balance that allowed the model to perform well across different scenarios while maintaining computational efficiency. This careful calibration was essential for achieving the desired model accuracy and robustness during the training process.

Data Augmentation Strategy

The data augmentation strategy is designed to enhance the model's robustness and generalization capability by simulating various camera movements and imperfections that might occur in real-world scenarios. This approach ensures the model is well-prepared to handle diverse and unpredictable situations. The augmentation strategy is applied with several considerations to maintain data integrity and ensure realistic training conditions. Augmentations are exclusively applied during the training stage to avoid influencing evaluation results, ensuring that the model's performance is assessed on clean, unaugmented data. Each sequence has a 50% probability of being augmented, which ensures a balanced mix of original and augmented data. This probabilistic approach prevents overfitting to any single type of augmentation. When augmentations are applied, they affect both input and output sequences consistently, maintaining temporal coherence and realism across the sequence, which is crucial for models learning from

sequential data. All augmented values are clipped to the range [0, 1], ensuring they remain valid normalised coordinates in the YOLO format. This clipping ensures that the augmented bounding boxes are usable within the model's expected input format. The data loading process also includes error handling mechanisms to manage any inconsistencies in the data, ensuring that training can continue even if individual samples are problematic.

Sequence Reversal

To effectively double the size of the training dataset, reversed sequences are included. For each original sequence $(S_1, S_2, \ldots, S_n)$, a corresponding reversed sequence $(S_n, S_{n-1}, \ldots, S_1)$ is added. This augmentation enables the model to learn to predict both forward and backward camera movements relative to the aircraft refuelling port, thereby enhancing its adaptability.

Camera Movement Simulation

Subtle camera movements are simulated to improve the model's robustness to varying camera positions. Panning is applied by introducing a smooth, cumulative random offset to the x and y coordinates of the bounding boxes, simulating the effect of the camera panning horizontally or vertically. The panning effect is modeled as:

$$\text{pan}_t = \sum_{i=1}^{t} \frac{N(0, \sigma^2)}{5}$$

where $N(0, \sigma^2)$ represents a normal distribution with a mean of 0 and variance σ^2. This simulation ensures the model can effectively handle gradual shifts in the camera's viewpoint.

Zoom Simulation

To account for changes in the apparent size of the refuelling port due to camera zoom or aircraft movement, a smooth, cumulative scaling factor is applied to the width and height of the bounding boxes. The zoom effect is modeled as:

$$\text{zoom}_t = \prod_{i=1}^{t} U(0.98, 1.02)$$

where $U(0.98, 1.02)$ is a uniform distribution between 0.98 and 1.02. This augmentation prepares the model to adapt to scenarios where the distance between the camera and the refuelling port changes dynamically.

Detection Inaccuracy Simulation

To enhance the model's resilience to slight inaccuracies in object detection, small Gaussian noise is added to all bounding box coordinates. This noise is sampled from $N(0, 0.002^2)$ for each coordinate, introducing minor variations that simulate real-world detection imperfections. Such noise mimics the slight inaccuracies that can occur in detection algorithms due to environmental factors or sensor noise.

4.4 Comparison Experiments

To evaluate the performance of the proposed *SizPos-GRU* model, a series of comparison experiments were conducted using several baseline models. These experiments are designed to assess the model's capability in predicting the future positions and sizes of the refuelling port in video sequences. The baseline models considered include the Linear Kalman Filter (LKF), Constant Velocity (CV) model, and variants of Recurrent Neural Networks (RNNs) such as Long Short-Term Memory (LSTM) and Gated Recurrent Unit (GRU).

Linear Kalman Filter (LKF)

The Linear Kalman Filter (LKF) is a recursive filter that estimates the state of a linear dynamic system from a series of incomplete and noisy measurements [36]. In the context of predicting the position of the refuelling port, the state vector $\mathbf{x}_t$ includes the position and velocity of the object. The model assumes constant velocity in the state transition, which is represented mathematically by the following equation:

$$\mathbf{x}_t = \mathbf{F}\mathbf{x}_{t-1} + \mathbf{w}_{t-1}, \tag{4.6}$$

In Equation (4.6), $\mathbf{F}$ is the state transition matrix that models how the state evolves from time $t-1$ to t, and $\mathbf{w}_{t-1}$ is the process noise, which accounts for any uncertainty in the system dynamics. The Kalman Filter also relies on an observation model to relate the state vector $\mathbf{x}_t$ to the actual measurements $\mathbf{z}_t$. This relationship is expressed as:

$$\mathbf{z}_t = \mathbf{H}\mathbf{x}_t + \mathbf{v}_t, \tag{4.7}$$

Here, in Equation (4.7), $\mathbf{H}$ is the observation matrix, which maps the true state space into the observed space, and $\mathbf{v}_t$ represents the measurement noise, capturing the inaccuracies in the sensor data. The Kalman Filter proceeds with two main steps: prediction and update. During the prediction step, the filter estimates the current state and its covariance based on the previous state:

$$\hat{\mathbf{x}}_{t|t-1} = \mathbf{F}\hat{\mathbf{x}}_{t-1|t-1}, \tag{4.8}$$

$$\mathbf{P}_{t|t-1} = \mathbf{F}\mathbf{P}_{t-1|t-1}\mathbf{F}^\top + \mathbf{Q}, \tag{4.9}$$

In Equation (4.8), $\hat{\mathbf{x}}_{t|t-1}$ denotes the predicted state at time t based on the state at time $t-1$, and $\mathbf{P}_{t|t-1}$ in Equation (4.9) represents the predicted covariance matrix, which quantifies the uncertainty in the predicted state. The matrix $\mathbf{Q}$ is the process noise covariance, reflecting the uncertainty in the system's evolution. In the update step, the filter adjusts the predicted state and covariance using the actual measurement $\mathbf{z}_t$ obtained at time t:

$$\mathbf{K}_t = \mathbf{P}_{t|t-1}\mathbf{H}^\top \left(\mathbf{H}\mathbf{P}_{t|t-1}\mathbf{H}^\top + \mathbf{R}\right)^{-1}, \tag{4.10}$$

$$\hat{\mathbf{x}}_{t|t} = \hat{\mathbf{x}}_{t|t-1} + \mathbf{K}_t\left(\mathbf{z}_t - \mathbf{H}\hat{\mathbf{x}}_{t|t-1}\right), \tag{4.11}$$

$$\mathbf{P}_{t|t} = \left(\mathbf{I} - \mathbf{K}_t\mathbf{H}\right)\mathbf{P}_{t|t-1}. \tag{4.12}$$

In Equation (4.10), $\mathbf{K}_t$ is the Kalman gain, which determines the weight given to the new measurement versus the predicted state. The updated state estimate $\hat{\mathbf{x}}_{t|t}$ in Equation (4.11) is

computed by correcting the predicted state $\hat{\mathbf{x}}_{t|t-1}$ with the measurement innovation (the difference between the actual and predicted measurements). Finally, the updated covariance $\mathbf{P}_{t|t}$, as shown in Equation (4.12), reflects the uncertainty in the updated state, incorporating the reduction in uncertainty achieved through the measurement update. The Kalman Filter iteratively performs these prediction and update steps, optimally combining prior knowledge and new measurements to provide a refined estimate of the refuelling port's position and velocity over time.

Constant Velocity (CV)

The Constant Velocity (CV) model assumes that the object continues to move at a constant speed and direction. This model is based on the principle that the object's motion remains uniform over time [65]. Given a sequence of past positions $\mathbf{P} = \{(x_1, y_1), \ldots, (x_T, y_T)\}$, the model first estimates the velocity $\mathbf{v}$ of the object. This velocity is computed by averaging the differences between consecutive positions:

$$\mathbf{v} = \frac{1}{T-1} \sum_{t=2}^{T} (\mathbf{P}_t - \mathbf{P}_{t-1}), \tag{4.13}$$

In Equation (4.13), $\mathbf{v}$ represents the average velocity, calculated over $T-1$ time steps, where $\mathbf{P}_t$ is the position at time t and $\mathbf{P}_{t-1}$ is the position at the previous time step. This average velocity assumes that the object has moved at a constant speed between each pair of consecutive positions. Once the velocity $\mathbf{v}$ is determined, the future positions $\mathbf{F}_k$ for k future steps can be predicted using the following equation:

$$\mathbf{F}_k = \mathbf{P}_T + k \cdot \mathbf{v}, \tag{4.14}$$

In Equation (4.14), $\mathbf{F}_k$ represents the predicted position of the object after k future time steps. The prediction is made by linearly extrapolating from the last observed position $\mathbf{P}_T$, with the object's position adjusted by the product of the velocity $\mathbf{v}$ and the number of time steps k into the future. This approach is straightforward and computationally efficient, making it useful for quick predictions in scenarios where the motion is relatively simple. However, its simplicity also means that it may be limited in handling more complex, dynamic, or non-linear motions, where the assumption of constant velocity does not hold true.

LSTM Model (PosVelAcc-LSTM)

The PosVelAcc-LSTM model leverages Long Short-Term Memory (LSTM) networks to predict future bounding box positions by encoding past positions, velocities, and accelerations. The model architecture is designed to capture the temporal dependencies in these input sequences, allowing for more accurate predictions of future movements. The architecture includes separate LSTM encoders for each input sequence (positions, velocities, and accelerations) and corresponding decoders for generating the predicted positions and velocities. This model was inspired by the PV-LSTM model from Bouhsain et al. [10]. The following algorithm outlines the process of the PosVelAcc-LSTM model:

Algorithm 1 PosVelAcc-LSTM Model

Require: $\mathbf{P}$ (position sequence), $\mathbf{V}$ (velocity sequence), $\mathbf{A}$ (acceleration sequence)
1: Encode past positions, velocities, and accelerations using LSTM encoders
2: Combine encoded states: $\mathbf{h}_{\text{combined}} = \mathbf{h}_P + \mathbf{h}_V + \mathbf{h}_A$
3: Initialise decoder inputs with the last observed position and velocity
4: **for** $t = 1$ to k **do** ▷ Predict for k future steps
5: Predict future position: $\hat{\mathbf{P}}_{t+1} = \text{LSTMDecoder}(\mathbf{h}_{\text{combined}})$
6: Predict future velocity: $\hat{\mathbf{V}}_{t+1} = \text{LSTMDecoder}(\mathbf{h}_{\text{combined}})$
7: **end for**
8: **return** Predicted positions and velocities

The model begins by encoding the sequences of past positions, velocities, and accelerations using separate LSTM encoders. The resulting hidden states $\mathbf{h}_P$, $\mathbf{h}_V$, and $\mathbf{h}_A$ are then combined into a unified representation $\mathbf{h}_{\text{combined}}$, which captures the joint temporal dependencies of these three input sequences. The decoding process starts with initialising the decoder inputs using the last observed position and velocity. For each future time step t (up to k steps), the model predicts the future position $\hat{\mathbf{P}}_{t+1}$ and velocity $\hat{\mathbf{V}}_{t+1}$ using the LSTM decoders, as shown in the algorithm. The training of the PosVelAcc-LSTM model is guided by minimising a composite loss function, which includes terms for both position and velocity predictions. This loss function is given by:

$$\mathscr{L}_{\text{total}} = \text{SmoothL1}(\hat{\mathbf{P}}, \mathbf{P}_{\text{true}}) + \text{SmoothL1}(\hat{\mathbf{V}}, \mathbf{V}_{\text{true}}), \tag{4.15}$$

In Equation (4.15), $\hat{\mathbf{P}}$ and $\hat{\mathbf{V}}$ represent the predicted positions and velocities, respectively, while $\mathbf{P}_{\text{true}}$ and $\mathbf{V}_{\text{true}}$ represent the corresponding ground truth values. The loss function uses the Smooth L1 loss (also known as Huber loss), which is robust to outliers and provides a balance between the L1 and L2 loss characteristics. By minimising $\mathscr{L}_{\text{total}}$, the model learns to accurately predict both the positions and velocities over the future time steps.

LSTM Model (SizPos-LSTM)

The SizPos-LSTM model extends the traditional LSTM architecture to predict both future bounding box positions and sizes. This model is specifically designed to handle two separate input sequences: the sequence of bounding box positions and the sequence of bounding box sizes. To achieve this, the model includes separate LSTM encoders for each type of sequence and corresponding decoders that predict future positions and sizes. The overall process of the SizPos-LSTM model can be outlined as follows:

Algorithm 2 SizPos-LSTM Model

Require: $\mathbf{P}$ (position sequence), $\mathbf{S}$ (size sequence)
1: Encode position and size using LSTM encoders
2: Combine encoded states: $\mathbf{h}_{\text{combined}} = \text{Combine}(\mathbf{h}_P, \mathbf{h}_S)$
3: Initialise decoder inputs with the last observed position and size
4: **for** $t = 1$ to k **do** ▷ Predict for k future steps
5: Predict future position: $\hat{\mathbf{P}}_{t+1} = \text{LSTMDecoder}(\mathbf{h}_{\text{combined}})$
6: Predict future size: $\hat{\mathbf{S}}_{t+1} = \text{LSTMDecoder}(\mathbf{h}_{\text{combined}})$
7: **end for**
8: **return** Predicted positions and sizes

The model begins by encoding the position sequence $\mathbf{P}$ and the size sequence $\mathbf{S}$ using separate LSTM encoders. The encoded hidden states, denoted as $\mathbf{h}_P$ for positions and $\mathbf{h}_S$ for sizes, are then combined into a unified representation $\mathbf{h}_{\text{combined}}$. This combined hidden state captures the temporal dependencies in both the positional and dimensional aspects of the bounding boxes. In the decoding phase, the model initialises the decoder inputs using the last observed position and size. It then iteratively predicts the future positions $\hat{\mathbf{P}}_{t+1}$ and sizes $\hat{\mathbf{S}}_{t+1}$ for each future time step t up to k steps, using the combined hidden state $\mathbf{h}_{\text{combined}}$. The training process for the SizPos-LSTM model involves minimising a composite loss function that includes terms for both position and size predictions. This loss function is expressed as:

$$\mathscr{L}_{\text{total}} = \text{SmoothL1}(\hat{\mathbf{P}}, \mathbf{P}_{\text{true}}) + \text{SmoothL1}(\hat{\mathbf{S}}, \mathbf{S}_{\text{true}}), \tag{4.16}$$

In Equation (4.16), $\hat{\mathbf{P}}$ and $\hat{\mathbf{S}}$ represent the predicted positions and sizes, respectively, while $\mathbf{P}_{\text{true}}$ and $\mathbf{S}_{\text{true}}$ represent the corresponding ground truth values. The loss function uses the Smooth L1 loss (also known as Huber loss), which balances sensitivity to outliers with the need to minimize large deviations. This composite loss $\mathscr{L}_{\text{total}}$ ensures that the model learns to accurately predict both the positions and sizes of bounding boxes over future time steps.

GRU Model (PosVelAcc)

The PosVelAcc-GRU model is similar to the PosVelAcc-LSTM model, but it utilises a Gated Recurrent Unit (GRU) network instead of LSTM for both encoding and decoding. GRUs are known for offering computational efficiency while maintaining the ability to capture temporal dependencies effectively, making them a suitable choice for sequence prediction tasks. This model is inspired by the Fusion-GRU model from Karim et al. [39]. The GRU model operates with the following key components:

$$\mathbf{z}_t = \sigma(\mathbf{W}_z \mathbf{x}_t + \mathbf{U}_z \mathbf{h}_{t-1}), \tag{4.17}$$

$$\mathbf{r}_t = \sigma(\mathbf{W}_r \mathbf{x}_t + \mathbf{U}_r \mathbf{h}_{t-1}), \tag{4.18}$$

$$\tilde{\mathbf{h}}_t = \tanh(\mathbf{W}_h \mathbf{x}_t + \mathbf{r}_t \odot \mathbf{U}_h \mathbf{h}_{t-1}), \tag{4.19}$$

$$\mathbf{h}_t = (1 - \mathbf{z}_t) \odot \mathbf{h}_{t-1} + \mathbf{z}_t \odot \tilde{\mathbf{h}}_t, \tag{4.20}$$

The update gate $\mathbf{z}_t$, as defined in Equation (4.17), controls the degree to which the previous hidden state $\mathbf{h}_{t-1}$ contributes to the current hidden state $\mathbf{h}_t$. This gate helps the model to decide how much past information should be passed forward to the next time step. The reset gate $\mathbf{r}_t$, shown in Equation (4.18), determines how much of the past information to forget. This gate is crucial in allowing the model to reset its memory selectively, enabling it to capture more complex temporal patterns. The candidate hidden state $\tilde{\mathbf{h}}_t$, calculated in Equation (4.19), represents the potential value for the new hidden state based on the current input $\mathbf{x}_t$ and the previous hidden state $\mathbf{h}_{t-1}$, modulated by the reset gate. Finally, the hidden state $\mathbf{h}_t$ at time t, given by Equation (4.20), is a linear interpolation between the previous hidden state $\mathbf{h}_{t-1}$ and the candidate hidden state $\tilde{\mathbf{h}}_t$, with the weights determined by the update gate $\mathbf{z}_t$. This final hidden state $\mathbf{h}_t$ encapsulates the temporal dependencies and is used in the decoding process to predict future positions and velocities. The PosVelAcc-GRU model leverages these mechanisms to efficiently process sequences of past positions, velocities, and accelerations, making it capable of generating accurate predictions for future bounding box positions and velocities while being computationally efficient.

4.5 Framework Evaluation

This framework integrates YOLOv10 for object detection and the *SizPos-GRU* model for future position prediction. The process begins by performing object detection across all frames of a video to establish ground truth for each frame. This pre-obtained ground truth simplifies the subsequent evaluation of prediction accuracy. The framework operates in a loop, where it first detects objects in 15 frames, then predicts their positions over the next 30 frames using the *SizPos-GRU* model. After each prediction phase, the next 15 frames are analysed for new detections, and this cycle repeats. By having the ground truth available from the outset, the framework allows for efficient evaluation of predictions, directly comparing predicted positions with known ground truth. The following pseudocode outlines the key steps of the framework:

Algorithm 3 Object Detection and Future Position Prediction Framework

```
procedure RunFramework(input_video_path, yolo_weights_path, gru_model_path, hparams_file, output_video_path, output_json_path, smoothing_filter, lkf, input_frames, future_frames)
    Load YOLOv10 model with yolo_weights_path
    Open video file at input_video_path
    detections ← []
    while frames in video do
        frame ← Read next frame
        results ← YOLOv10.detect(frame)
        detections ← Extract bounding boxes from results
    end while
    Store detections as ground truth for all frames
    Initialise loop to process detections in segments
    while more detections to process do
        segment_detections ← Take next input_frames from detections
        track_history_bbox ← Update with segment_detections
        if track_history_bbox is full then
            predicted_positions ← GRU.predict(track_history_bbox)
            if lkf is True then
                predicted_positions ← Apply Kalman Filter to predicted_positions
            end if
            smoothed_combined_bboxes ← Apply chosen smoothing_filter to predicted_positions
            for each future frame in future_frames do
                Calculate prediction metrics (e.g., ADE, FDE, IoU)
                Annotate frame with current, predicted, and ground-truth bounding boxes
            end for
        end if
        Continue to next input_frames in detections
    end while
    Save annotated video to output_video_path
    Save prediction metrics and smoothed detections to output_json_path
end procedure
```

Chapter 5

Results and Discussion

5.1 Object Detection Training Results

This section presents the final testing results of three different YOLO models—YOLOv10n.pt, YOLOv10s.pt, and YOLOv10m.pt—on a dataset focused on classifying fuel port states (CLOSED, SEMI-OPEN, OPEN). The evaluation considers key performance metrics, including Precision (P), Recall (R), mean Average Precision at 50% IoU (mAP50), and mean Average Precision across multiple IoU thresholds (mAP50-95).

Table 5.1: Performance comparison of finetuned YOLO models on the detection of Refuelling Port.

Model	Metric	All	Fuel Port [CLOSED]	Fuel Port [SEMI-OPEN]	Fuel Port [OPEN]
YOLOv10n.pt	Precision (P)	0.989	0.994	0.982	**0.992**
	Recall (R)	0.876	0.657	0.996	0.974
	mAP50	**0.893**	0.696	0.995	0.987
	mAP50-95	**0.852**	0.684	0.962	**0.909**
YOLOv10s.pt	Precision (P)	**0.997**	**0.998**	**1.000**	**0.992**
	Recall (R)	0.884	**0.682**	0.997	0.974
	mAP50	**0.893**	0.694	**0.995**	**0.989**
	mAP50-95	0.848	0.678	0.961	0.905
YOLOv10m.pt	Precision (P)	0.994	0.996	0.999	0.988
	Recall (R)	**0.888**	**0.682**	**1.000**	**0.983**
	mAP50	0.892	**0.701**	**0.995**	0.981
	mAP50-95	**0.852**	**0.692**	**0.968**	0.897

The object detection performance of the three YOLO models was evaluated based on their ability to detect the aircraft refuelling port in its different states: CLOSED, SEMI-OPEN, and OPEN. Table 5.1 provides a comprehensive comparison across various metrics, with certain values highlighted in bold to signify the best performance for each specific metric across the models. The bold values in the table indicate the highest scores within each metric category, either across all states or within specific fuel port states. These bold values highlight the model that performed the best for that particular metric (Precision, Recall, mAP50, mAP50-95) in the corresponding category (All, CLOSED, SEMI-OPEN, OPEN). The comparison is made on a row-by-row basis. For each row representing a specific performance metric, the values are compared across the three models (YOLOv10n.pt, YOLOv10s.pt, YOLOv10m.pt). For instance, YOLOv10s.pt exhibited the highest precision overall at 0.997, as well as the highest precision

across all fuel port states, indicating its strong ability to correctly identify true positives while minimising false positives. On the other hand, YOLOv10m.pt outperformed the others in terms of recall, achieving a score of 0.888 and recording the highest recall for the SEMI-OPEN and OPEN states. This suggests that YOLOv10m.pt is more effective at capturing true positives, making it ideal for scenarios where it is crucial not to miss any detections. Additionally, both YOLOv10n.pt and YOLOv10m.pt achieved the highest mAP50-95 scores at 0.852, demonstrating balanced performance across different IoU thresholds. These results highlight the strengths of each model depending on the specific metric and category, underscoring the importance of selecting the appropriate model based on the specific needs of the application—whether prioritizing precision, recall, or overall balanced performance across different IoU thresholds.

5.2 Experiment Results

This section details the outcomes of the experiments conducted to evaluate the performance of various models in predicting the future position of the aircraft refuelling port. The analysis covers evaluation metrics, hyperparameter tuning outcomes, and model comparisons, highlighting the effectiveness and robustness of the proposed methods.

5.2.1 Hyperparameter Tuning

Hyperparameter tuning was conducted to optimise the performance of the *SizPos-GRU* model. The experiments evaluated different combinations of hidden sizes and hidden depths to determine their impact on key performance metrics: Average Displacement Error (ADE), Final Displacement Error (FDE), Average Intersection over Union (AIoU), and Final Intersection over Union (FIoU). As presented in Tables 5.2 and 5.3, the results indicate that certain configurations lead to significantly better performance. In Table 5.2, which details the results for predicting 60 frames into the future using data from the previous 30 frames, the best performance was achieved with a hidden size of 128 and a hidden depth of 8. This configuration resulted in an ADE of 32.7 pixels and an FDE of 73.3 pixels. These values, highlighted in bold, indicate the lowest errors among all tested configurations for this scenario. Additionally, this setup yielded high AIoU and FIoU scores, which are also bolded to signify their superior overlap with ground truth data. Similarly, Table 5.3 presents the tuning results for predicting 30 frames into the future using data from the previous 15 frames. Here, a hidden size of 256 and a hidden depth of 8 produced the best results, with an ADE of 17.2 pixels and an FDE of 38.6 pixels, both highlighted in bold to denote their excellence. The corresponding AIoU and FIoU values are also bolded, indicating strong model accuracy. The bold values in both tables represent the best-performing configurations for each metric, emphasizing the configurations that yielded the lowest errors and highest IoU scores. These findings underscore the importance of carefully selecting hyperparameters to enhance the model's predictive capabilities. The variation in performance across different temporal windows further suggests that the model's sensitivity to the length of the prediction horizon should be taken into consideration in future applications. This comprehensive hyperparameter tuning process highlights how different configurations can significantly impact the model's accuracy, with the bolded values guiding the selection of optimal settings for the *SizPos-GRU* model.

Table 5.2: Hyperparameter tuning results for trajectory prediction using *SizPos-GRU* model that leverages 30 past frames (1 sec) to predict the position 60 frames (2 sec) into the future.

Hidden Size	Hidden Depth	ADE (pxl)	FDE (pxl)	AIoU (%)	FIoU (%)
32	1	43.3	90.1	39.4	11.5
32	3	44.6	88.5	36.5	13.2
32	6	44.0	79.9	36.9	18.7
32	8	39.2	81.8	40.0	16.1
64	1	53.4	98.6	35.1	13.9
64	3	42.8	87.1	41.2	17.7
64	6	37.0	82.1	44.9	18.5
64	8	35.8	78.8	44.0	18.8
128	1	56.7	96.5	33.3	13.7
128	3	40.9	92.0	43.6	17.5
128	6	32.4	80.9	47.7	16.0
128	**8**	**32.7**	**73.3**	**47.6**	**20.6**
256	1	41.2	86.8	41.5	19.6
256	3	34.0	79.0	47.0	17.5
256	6	35.7	85.0	47.1	17.6
256	8	34.5	82.6	46.2	17.7
512	1	38.3	79.8	44.0	17.3
512	6	35.9	82.7	44.7	18.1
512	8	39.0	81.5	42.5	15.9

Table 5.3: Hyperparameter tuning results for trajectory prediction using *SizPos-GRU* model that leverages 15 past frames (0.5 sec) to predict the position 30 frames (1 sec) into the future.

Hidden Size	Hidden Depth	ADE (pxl)	FDE (pxl)	AIoU (%)	FIoU (%)
32	1	23.0	45.6	58.3	35.9
32	2	23.5	46.3	58.2	34.0
32	4	28.0	59.7	58.5	33.9
32	8	23.3	45.1	56.9	36.3
64	1	29.8	55.2	58.4	35.8
64	2	31.0	56.9	57.1	33.5
64	4	21.2	45.1	61.4	37.4
64	8	20.1	44.1	62.1	39.6
128	1	25.1	48.4	58.6	37.9
128	2	26.6	49.2	50.6	31.4
128	4	25.4	53.6	60.1	33.8
128	8	18.7	42.4	62.5	37.3
256	1	28.0	55.9	58.1	36.5
256	2	22.2	52.0	62.6	35.6
256	4	20.3	50.6	62.8	33.3
256	**8**	**17.2**	**38.6**	**62.4**	**39.4**
512	1	22.8	45.1	58.8	35.3
512	2	27.8	52.0	54.7	34.6
512	4	19.4	43.0	60.2	36.8
512	8	19.3	44.2	60.7	34.0

The *SizPos-GRU* model's performance was evaluated against various baseline models in two distinct scenarios: predicting 60 frames into the future using data from the previous 30 frames, and predicting 30 frames into the future using data from the previous 15 frames. The models were assessed based on key performance metrics including Average Displacement Error (ADE) and Final Displacement Error (FDE), both reported in pixels and as a percentage of the maximum possible error, as well as Average Intersection over Union (AIoU) and Final Intersection over Union (FIoU). In the 60-frame prediction task (Table 5.4), the *SizPos-GRU* model demonstrated superior accuracy, achieving the lowest ADE (34.2 pixels, 4.28%) and FDE (73.4 pixels, 9.18%) among the tested models. These results indicate the model's strong capability in predicting future positions with minimal deviation from the ground truth. Although the FIoU value of 22.1% reflects moderate spatial overlap, the low displacement errors underscore the model's effectiveness in minimising prediction deviations. Tables 5.5 and 5.4 present a comparison of traditional baseline models (CV and LKF) and various customised models that were developed in this study, separated by a dashed line. The models below the dashed line represent customised versions that use different selections of model architectures and hyperparameters. These include variations of Long Short-Term Memory (LSTM) networks and Gated Recurrent Units (GRU), each designed to enhance the trajectory prediction capabilities. The *SizPos-GRU* model, in particular, was trained to achieve the best performance among these custom models. Similarly, in the 30-frame prediction task (Table 5.5), the *SizPos-GRU* model excelled with an ADE of 17.2 pixels (2.15%) and an FDE of 38.6 pixels (4.83%). These results, particularly the low ADE and FDE, confirm the model's reliability in short-term predictions. While the FIoU metric may be less critical for the application of this thesis, the low displacement errors validate the model's performance, making it a robust choice for tasks that require precise trajectory prediction.

Table 5.4: Performance comparison of various models on trajectory prediction tasks using 30 past frames to predict 60 future frames.

Model	**ADE (pxl)**	**ADE (%)**	**FDE (pxl)**	**FDE (%)**	**AIoU (%)**	**FIoU (%)**
CV [65]	129.6	16.2%	268.4	33.6%	25.6	9.0
LKF [36]	110.9	13.9%	251.5	31.4%	30.1	6.4
PosVelAcc-LSTM	69.1	8.6%	115.0	14.4%	26.6	11.2
SizPos-LSTM	49.7	6.2%	95.7	12.0%	41.3	15.7
PosVelAcc-GRU	81.5	10.2%	121.3	15.2%	23.3	10.7
SizPos-GRU	**34.2**	**4.28%**	**73.4**	**9.18%**	**46.5**	**22.1**

Table 5.5: Performance comparison of various models on trajectory prediction tasks using 15 past frames to predict 30 future frames.

Model	**ADE (pxl)**	**ADE (%)**	**FDE (pxl)**	**FDE (%)**	**AIoU (%)**	**FIoU (%)**
CV [65]	49.9	6.2%	107.7	13.5%	45.3	20.2
LKF [36]	42.8	5.4%	97.5	12.2%	49.2	21.9
PosVelAcc-LSTM	41.8	5.2%	79.0	9.9%	42.4	20.0
SizPos-LSTM	25.3	3.2%	49.9	6.2%	58.8	36.1
PosVelAcc-GRU	39.2	4.9%	77.1	9.6%	46.3	23.1
SizPos-GRU	**17.2**	**2.15%**	**38.6**	**4.83%**	**62.4**	**39.4**

5.2.2 Framework Evaluation

To comprehensively assess the trajectory prediction framework's performance, various smoothing filters and Linear Kalman Filter (LKF) configurations were tested across three different video datasets: *test_indoor1* (Table 5.6) *video_lab_semiopen_1_3* (Table 5.7), and *video_lab_platform_6* (Table 5.8). The primary metrics evaluated include Average Displacement Error (ADE), Final Displacement Error (FDE), Average Intersection over Union (AIoU), and Final Intersection over Union (FIoU), each providing insight into the accuracy and reliability of the prediction models. In the *test_indoor1* dataset (Table 5.6), the Savitzky-Golay filter combined with LKF achieved an ADE of 80.44 pixels and an FDE of 128.70 pixels. This configuration showed competitive performance, particularly in maintaining a balance between spatial overlap and prediction accuracy, as indicated by an AIoU of 22.53% and an FIoU of 5.99%. However, when LKF was disabled, the Savitzky-Golay filter further improved the ADE to 76.48 pixels, suggesting that in some scenarios, the smoothing effect of the filter can independently enhance prediction accuracy without the need for LKF. Interestingly, the Exponential Smoothing filter, whether used with or without LKF, consistently produced higher ADE and FDE values, with a noticeable drop in AIoU and FIoU, highlighting its less effective handling of trajectory prediction in dynamic indoor environments. The results from the *video_lab_semiopen_1_3* dataset (Table 5.7) reveal similar trends. The Savitzky-Golay filter, when not paired with LKF, achieved the best overall performance with an ADE of 69.75 pixels and an FDE of 105.15 pixels, along with the highest FIoU value of 11.16%. This suggests that in semi-open environments, where conditions may vary, the Savitzky-Golay filter excels at maintaining prediction accuracy and consistency. Conversely, the Hybrid filter performed poorly in this scenario, particularly without LKF, where it resulted in an FDE as high as 157.37 pixels and an FIoU of just 0.16%, indicating a significant reduction in predictive reliability. The analysis of the *video_lab_platform_6* dataset (Table 5.8) further reinforces the effectiveness of the Savitzky-Golay filter. This filter, when used without LKF, provided the lowest ADE of 32.45 pixels and a competitive FDE of 58.12 pixels, coupled with the highest AIoU (48.56%) and FIoU (28.27%) values. These metrics suggest that in platform-based scenarios, where the environment may be more controlled or predictable, the Savitzky-Golay filter can significantly enhance the model's ability to track and predict the trajectory of the refuelling port. In contrast, the Moving Average and Gaussian filters, although relatively close in performance, failed to match the superior accuracy demonstrated by the Savitzky-Golay filter. Overall, the results across all three videos indicate that the Savitzky-Golay filter, both with and without LKF, consistently provides the most reliable predictions. Its ability to preserve important trajectory trends while effectively filtering out noise allows for more accurate and stable predictions, as reflected by the lower ADE and FDE values and higher intersection-over-union metrics. The less favourable performance of other filters, particularly in varying environmental conditions, underscores the importance of selecting the appropriate smoothing technique based on the specific characteristics of the application environment. The combination of these findings suggests that the Savitzky-Golay filter, especially when applied in conjunction with LKF in dynamic environments, offers a robust solution for enhancing the predictive performance of trajectory models in automated aircraft refuelling systems.

Table 5.6: Performance metrics using different smoothing filters and Linear Kalman Filter (LKF) configurations for video test_indoor1.

Smooth Filter	**LKF**	**ADE (px)**	**ADE (%)**	**FDE (px)**	**FDE (%)**	**AIoU (%)**	**FIoU (%)**
Savitzky-Golay	True	80.44	10.05	128.70	16.09	22.53	5.99
Moving Average	True	81.94	10.24	127.64	15.95	22.14	6.60
Exponential Smoothing	True	92.94	11.62	137.84	17.23	18.54	5.66
Hybrid	True	83.05	10.38	205.58	25.70	22.32	0.10
Gaussian	True	81.26	10.16	128.80	16.10	22.04	5.95
No Smoothing	True	81.74	10.22	**127.57**	**15.95**	21.84	7.20
Savitzky-Golay	False	**76.48**	**9.56**	127.81	15.98	26.68	6.67
Moving Average	False	77.24	9.65	128.77	16.10	**26.70**	6.81
Exponential Smoothing	False	88.59	11.07	136.42	17.05	21.15	**9.65**
Hybrid	False	78.91	9.86	200.46	25.06	26.46	0.00
Gaussian	False	76.90	9.61	128.77	16.10	26.57	7.36
No Smoothing	False	77.11	9.64	128.23	16.03	26.30	6.53

Table 5.7: Performance metrics using different smoothing filters and Linear Kalman Filter (LKF) configurations for video *video_lab_semiopen_1_____3*.

Smooth Filter	**LKF**	**ADE (px)**	**ADE (%)**	**FDE (px)**	**FDE (%)**	**AIoU (%)**	**FIoU (%)**
Savitzky-Golay	True	71.81	8.98	107.74	13.47	19.93	6.54
Moving Average	True	72.70	9.09	108.05	13.51	20.05	7.19
Exponential Smoothing	True	81.95	10.24	114.07	14.26	18.57	6.97
Hybrid	True	73.66	9.21	163.35	20.42	19.70	0.24
Gaussian	True	72.25	9.03	108.29	13.54	19.90	7.19
No Smoothing	True	72.66	9.08	107.62	13.45	19.57	7.26
Savitzky-Golay	False	**69.75**	**8.72**	**105.15**	**13.14**	21.94	**11.16**
Moving Average	False	70.20	8.78	105.90	13.24	**22.20**	10.41
Exponential Smoothing	False	79.99	10.00	113.54	14.19	18.98	7.96
Hybrid	False	71.52	8.94	157.37	19.67	21.54	0.16
Gaussian	False	70.07	8.76	106.43	13.30	21.89	10.93
No Smoothing	False	70.09	8.76	106.23	13.28	22.03	10.14

Table 5.8: Performance metrics using different smoothing filters and Linear Kalman Filter (LKF) configurations for video *video_lab_platform_6*.

Smooth Filter	**LKF**	**ADE (px)**	**ADE (%)**	**FDE (px)**	**FDE (%)**	**AIoU (%)**	**FIoU (%)**
Savitzky-Golay	True	34.29	4.29	**57.98**	**7.25**	45.91	26.97
Moving Average	True	34.84	4.35	58.33	7.29	45.24	27.39
Exponential Smoothing	True	38.57	4.82	59.30	7.41	41.63	27.76
Hybrid	True	36.40	4.55	120.79	15.10	45.08	1.52
Gaussian	True	34.51	4.31	58.26	7.28	45.54	27.54
No Smoothing	True	35.05	4.38	59.23	7.40	44.77	26.72
Savitzky-Golay	False	**32.45**	**4.06**	58.12	7.26	**48.56**	28.27
Moving Average	False	32.62	4.08	58.85	7.36	48.41	**28.96**
Exponential Smoothing	False	37.08	4.63	59.86	7.48	42.91	28.34
Hybrid	False	34.50	4.31	119.97	15.00	47.66	2.32
Gaussian	False	32.54	4.07	58.69	7.34	48.40	28.70
No Smoothing	False	32.66	4.08	58.82	7.35	48.31	28.89

5.3 Testing Visualisation

This section analyses the trajectory prediction framework's performance using three distinct video datasets: *video_lab_platform_6*, *video_lab_semiopen_1_____3*, and *test_indoor1*. The objective is to assess the accuracy and reliability of the framework's predictions under varying motion scenarios.

5.3.1 Framework Output Visualisation

Figure 5.1 illustrates the predicted and ground truth central positions of the refuelling port across different frame sequences. The visualisation employs bounding boxes to represent current, predicted, and ground truth positions, where the red, green, and blue boxes correspond to the current position, predicted future position, and ground truth future position, respectively. The alignment between the green and blue boxes serves as an indicator of the model's prediction accuracy. Misalignments, where the boxes diverge, highlight instances of prediction error, which may stem from model limitations or complexities in the motion dynamics. The figure is organised into rows and columns to facilitate comparative analysis across different videos and frame sequences, enabling an assessment of the model's robustness and adaptability across varied conditions.

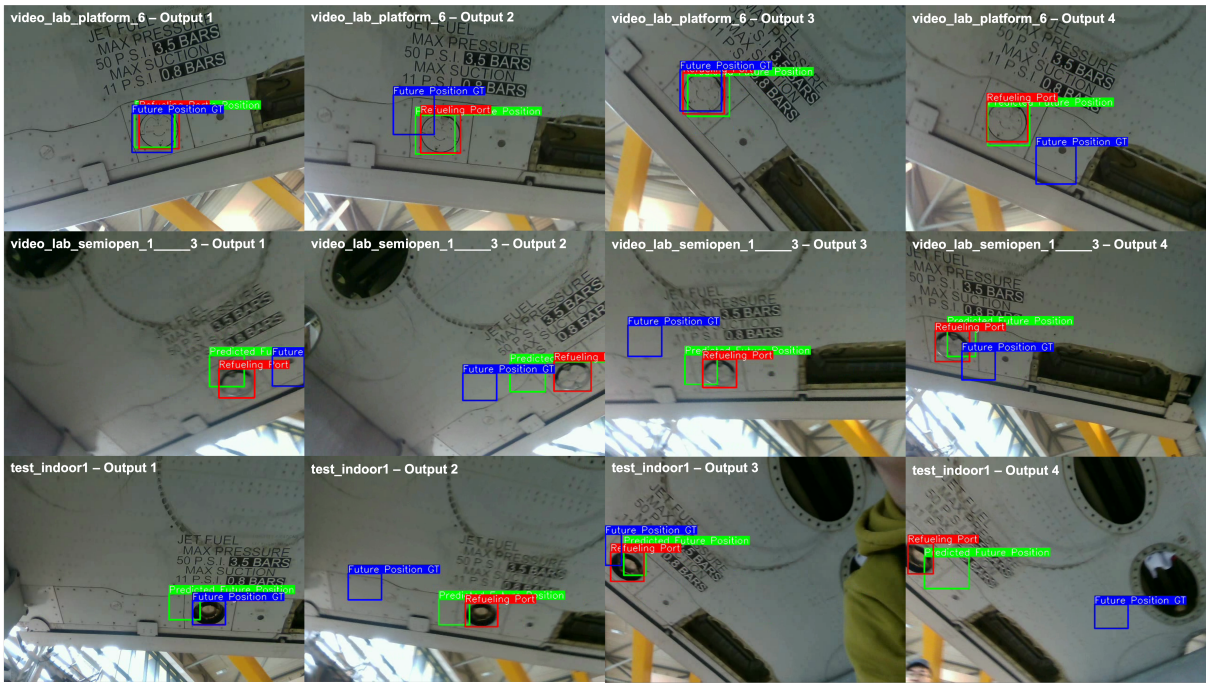

Figure 5.1: Visualisation of the trajectory prediction framework output for videos *video_lab_platform_6*, *video_lab_semiopen_1_____3*, and *test_indoor1*.

5.3.2 Framework Output Analysis

Figures 5.2, 5.3, and 5.4 compare the predicted motion trajectories against the ground truth, providing insight into the model's predictive performance. The ground truth X and Y coordinates are depicted by black dash-dot and dotted lines, respectively, serving as reference benchmarks. The predictions are presented using various filtering methods: raw data predictions (blue), Savitzky-Golay (SG) filtered predictions (green), and predictions filtered with a combination of Linear Kalman Filter (LKF) and SG (orange). In Figure 5.2, predictions for *video_lab_platform_6* across three frame intervals (61 to 90, 106 to 135, and 151 to 180) reveal that the framework closely tracks the ground truth when filters are applied. The SG and LKF-SG filters significantly reduce noise, resulting in smoother trajectories that align closely with the actual motion path. However, the raw predictions exhibit considerable variability, particularly in the latter frames, indicating the model's sensitivity to noise and its limitations in unfiltered scenarios. Despite the enhanced accuracy from filtering, a slight lag in prediction responsiveness is observed, which could affect the framework's performance in tracking rapid motion changes. Figure 5.3 extends this analysis to *video_lab_semiopen_1_____3*. Here, the framework demonstrates robustness in maintaining prediction accuracy across various motion dynamics. Filtered predictions consistently align with the ground truth, particularly under stable motion conditions. However, the raw predictions show greater variability, indicating challenges in accurately predicting abrupt or irregular motion without the support of filters. This suggests that while the framework is effective in stable conditions, its performance may diminish in more dynamic environments. Finally, Figure 5.4 evaluates the framework's performance on the *test_indoor1* dataset. Even in a more constrained and complex environment, the filtered predictions maintain close alignment with the ground truth, especially with the LKF-SG filter. However, discrepancies are observed during rapid motion transitions, indicating that while filtering enhances prediction accuracy, the framework may struggle to capture sudden changes in motion fully. Overall, the analysis highlights that the trajectory prediction framework performs well under certain conditions, particularly when filtering techniques are employed to mitigate noise and improve accuracy. However, the model's dependence on filtering also reveals its sensitivity to noise and its limitations in predicting rapid or irregular motion patterns.

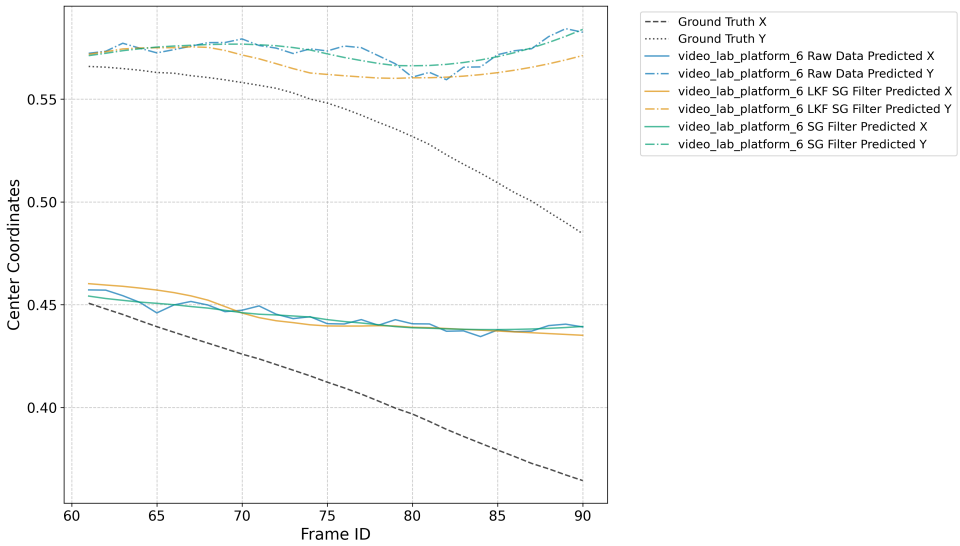

(a) Predictions from frame 61 to 90.

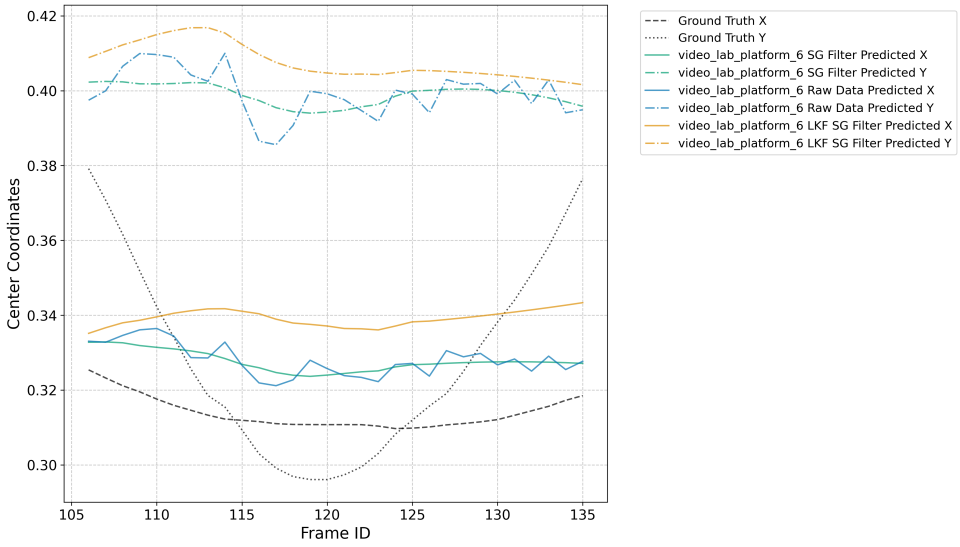

(b) Predictions from frame 106 to 135.

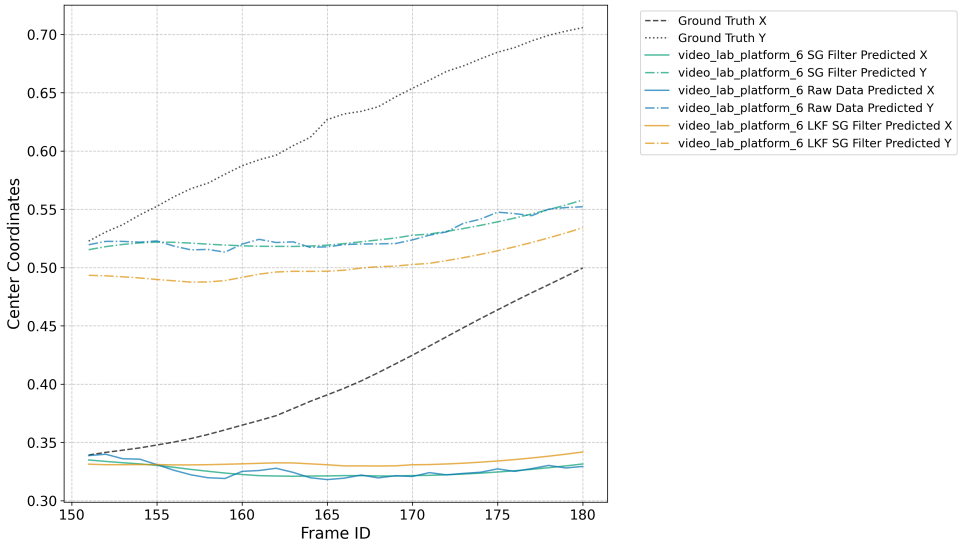

(c) Predictions from frame 151 to 180.

Figure 5.2: Framework outputs from frame 61 to 90 for video *video_lab_platform_6*.

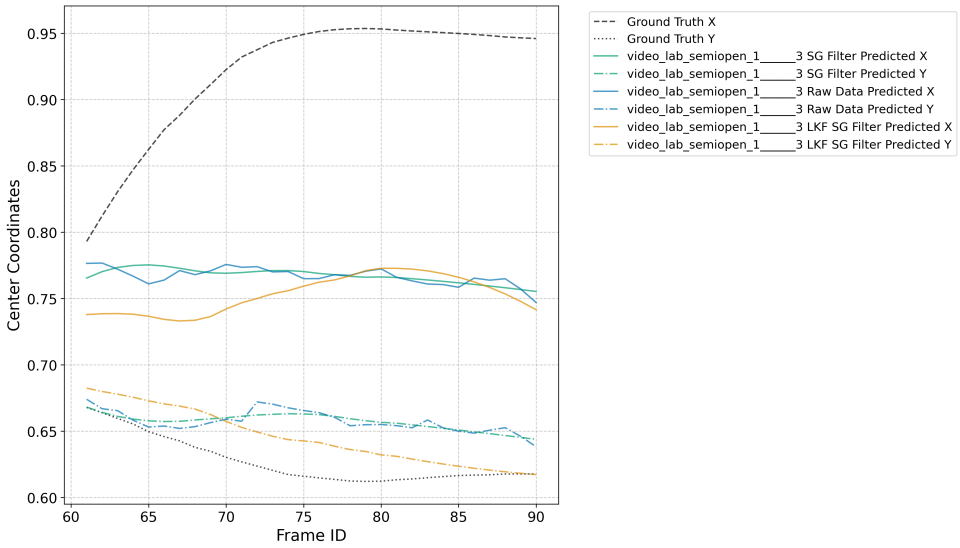

(a) Predictions from frame 61 to 90.

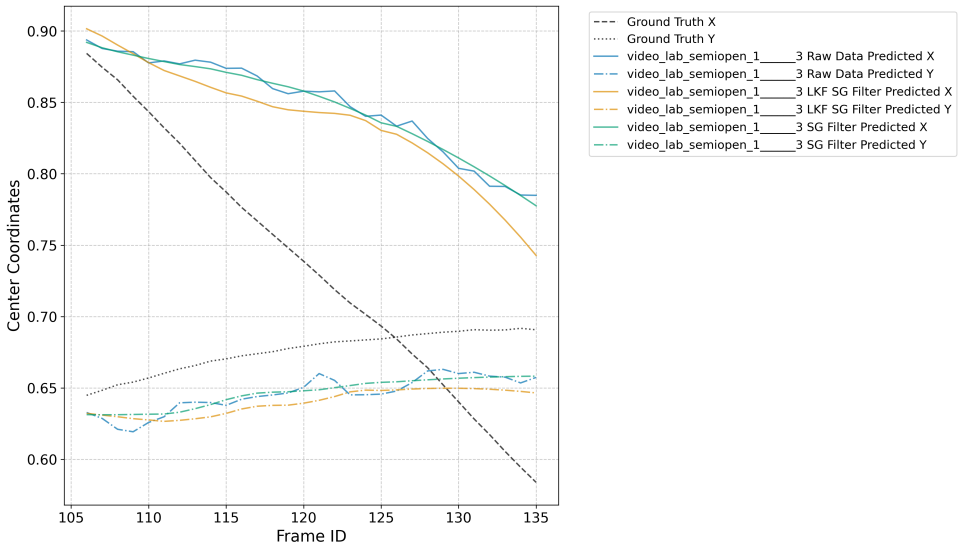

(b) Predictions from frame 106 to 135.

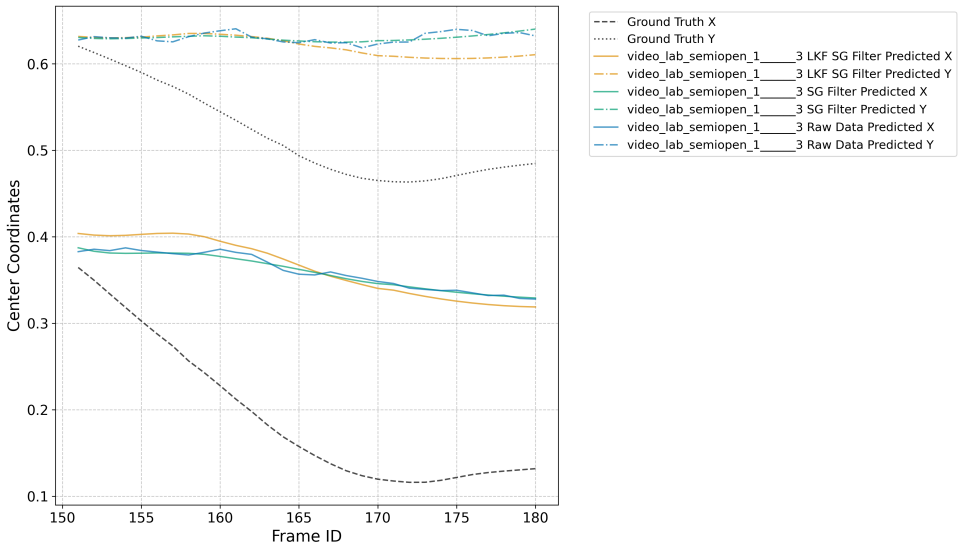

(c) Predictions from frame 151 to 180.

Figure 5.3: Framework outputs from frame 61 to 180 for video *video_lab_semiopen_1_____3*.

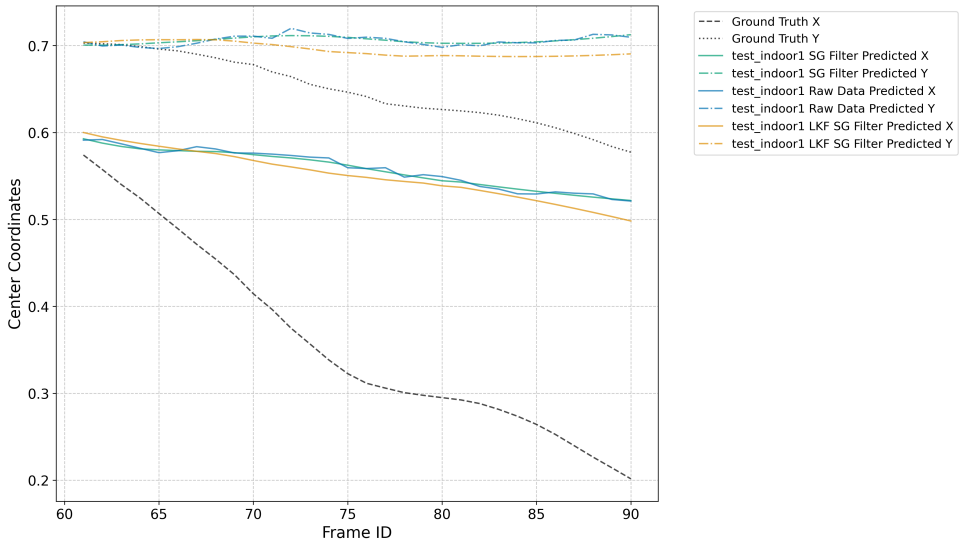

(a) Predictions from frame 61 to 90.

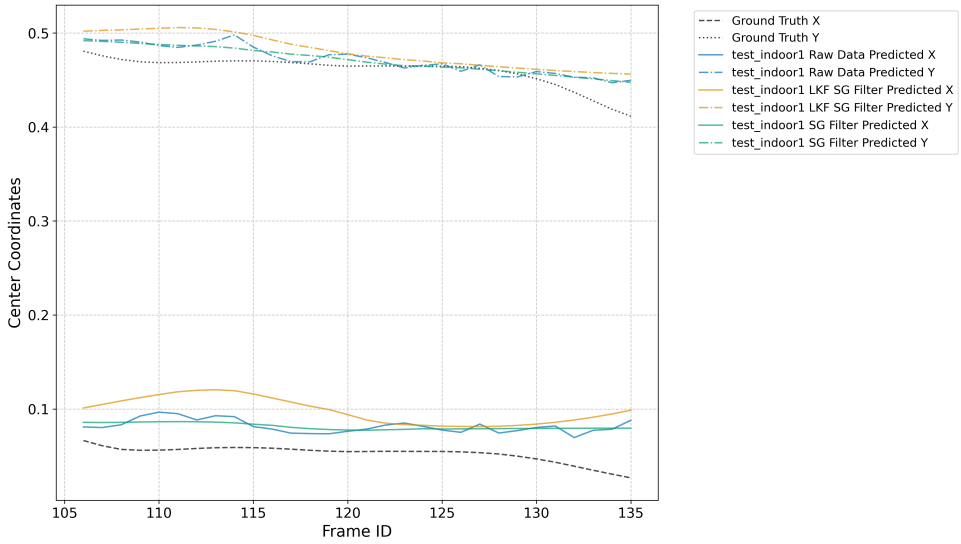

(b) Predictions from frame 106 to 135.

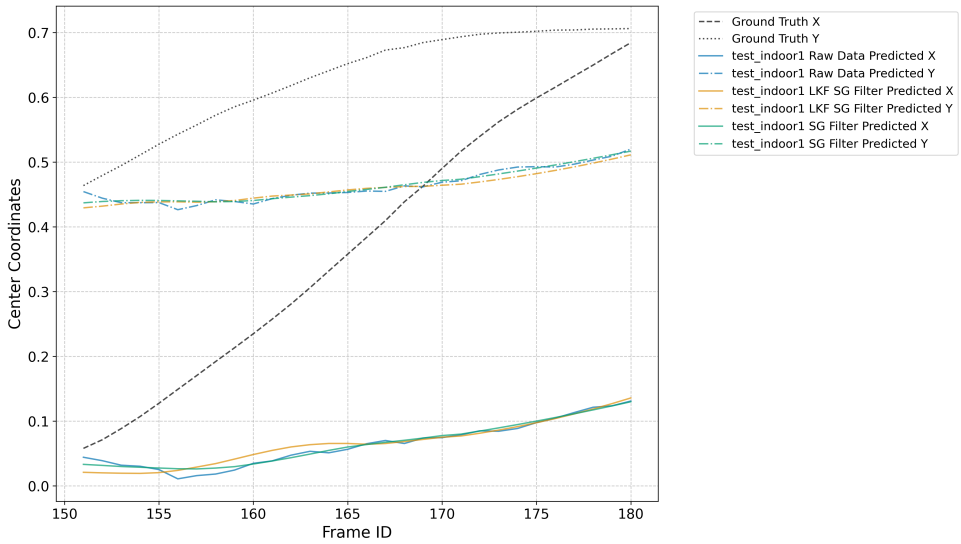

(c) Predictions from frame 151 to 180.

Figure 5.4: Framework outputs from frame 61 to 180 for video *test_indoor1*.

Chapter 6

Conclusion and Future Work

6.1 Summary

This thesis has developed and evaluated a future position prediction framework specifically designed for the automated refuelling of commercial aircraft. The research has addressed critical challenges in detecting and predicting the position of refuelling ports, which are often obscured by factors such as motion blur, occlusion, or complex environmental conditions. By leveraging advanced deep learning techniques, including the *SizPos-GRU* model combined with a fine-tuned YOLOv10 object detection system, the framework demonstrates significant improvements in predictive accuracy and reliability across various scenarios. The experimental results highlight the efficacy of integrating temporal and spatial data for robust object tracking and motion prediction, thus contributing to the advancement of automated aircraft ground operations.

6.2 Technological Contributions

The thesis makes several technological contributions. The design and implementation of the *SizPos-GRU* model represents a novel approach to capturing temporal dependencies and spatial relationships within video streams. This model's encoder-attention-decoder architecture has been shown to ensure accurate predictions of future positions and sizes of aircraft refuelling ports. Furthermore, the integration of the *SizPos-GRU* model with a fine-tuned YOLOv10 object detection system provides a comprehensive solution for detecting, tracking, and predicting the trajectory of refuelling ports in dynamic environments. Advanced filtering techniques, including the Savitzky-Golay filter combined with Kalman Filters, have been implemented to significantly enhance the stability and reliability of the model's predictions by reducing noise and smoothing the trajectories. Additionally, a specialised dataset has been created and annotated, capturing various states of the refuelling port under different lighting and environmental conditions. This dataset serves as a valuable resource for training and evaluating deep learning models in this domain.

6.3 Future Work

While the proposed framework has demonstrated promising results, several areas warrant further exploration and development. Future research should focus on optimising the model's processing speed to enable real-time implementation in operational environments, which would

involve reducing the computational complexity of the framework while maintaining accuracy. Expanding the framework's applicability by training and testing it in a wider range of environmental conditions and aircraft models is also crucial. This could involve collecting more diverse datasets to improve the model's generalisation capabilities. Moreover, enhancing the model's robustness in handling abrupt motion changes and irregular patterns is necessary. This could be achieved by integrating more sophisticated recurrent architectures or exploring hybrid models that combine deep learning with traditional computer vision techniques. Investigating methods to extend the prediction horizon while maintaining accuracy is another important direction for future work, as this is crucial for improving the anticipation of future positions in dynamic and unpredictable environments.

References

1. A. Alahi, K. Goel, V. Ramanathan, A. Robicquet, L. Fei-Fei, and S. Savarese. Social lstm: Human trajectory prediction in crowded spaces. volume 2016-December, 2016. doi: 10.1109/CVPR.2016.110.

2. S. Alemany, J. Beltran, A. Perez, and S. Ganzfried. Predicting hurricane trajectories using a recurrent neural network. 2019. doi: 10.1609/aaai.v33i01.3301468.

3. J. Ansel, E. Yang, H. He, N. Gimelshein, A. Jain, M. Voznesensky, B. Bao, P. Bell, D. Berard, E. Burovski, G. Chauhan, A. Chourdia, W. Constable, A. Desmaison, Z. DeVito, E. Ellison, W. Feng, J. Gong, M. Gschwind, B. Hirsh, S. Huang, K. Kalambarkar, L. Kirsch, M. Lazos, M. Lezcano, Y. Liang, J. Liang, Y. Lu, C. Luk, B. Maher, Y. Pan, C. Puhrsch, M. Reso, M. Saroufim, M. Y. Siraichi, H. Suk, M. Suo, P. Tillet, E. Wang, X. Wang, W. Wen, S. Zhang, X. Zhao, K. Zhou, R. Zou, A. Mathews, G. Chanan, P. Wu, and S. Chintala. PyTorch 2: Faster Machine Learning Through Dynamic Python Bytecode Transformation and Graph Compilation. In *29th ACM International Conference on Architectural Support for Programming Languages and Operating Systems, Volume 2 (ASPLOS '24)*. ACM, Apr. 2024. doi: 10.1145/3620665.3640366. URL https://pytorch.org/assets/pytorch2-2.pdf.

4. A. F. C. A. C. A. . M. C. (AvMC). Ar3p program background (2017-2019) and robotic hot refueling demonstrations (sep-oct 2020), 2020. URL hhttps://www.denix.osd.mil/ndcee/denix-files/sites/44/2023/09/EXSUM-AR3P-Robotic-Refueling-K-MAX-and-S-70-Sep_Oct-2020-v9.pdf. Accessed: 2024-06-24.

5. J. Bailey. What is fuel tankering and why should you care?, 2019. URL https://simpleflying.com/fuel-tankering/. Accessed: 2024-06-24.

6. A. Bemporad. Recurrent neural network training with convex loss and regularization functions by extended kalman filtering. *IEEE Transactions on Automatic Control*, 68, 2023. ISSN 15582523. doi: 10.1109/TAC.2022.3222750.

7. R. A. Bennett, Y. C. Shiu, and M. B. Leahy. A robust light invariant vision system for aircraft refueling. volume 1, 1991. doi: 10.1109/robot.1991.131568.

8. S. Blakey, L. Rye, and C. W. Wilson. Aviation gas turbine alternative fuels: a review. *Proceedings of the Combustion Institute*, 33(2):2863–2885, 2011. doi: 10.1016/j.proci.2010.09.011.

9. A. Bochkovskiy, C. Wang, and H. M. Liao. Yolov4: Optimal speed and accuracy of object detection. *CoRR*, abs/2004.10934, 2020. URL https://arxiv.org/abs/2004.10934.

10. S. A. Bouhsain, S. Saadatnejad, and A. Alahi. Pedestrian intention prediction: A multi-task perspective. *CoRR*, abs/2010.10270, 2020. URL https://arxiv.org/abs/2010.10270.

11. H. Burnette. Lab demonstrates robotic ground refueling of aircraft, Oct. 2010. URL https://www.wpafb.af.mil/News/Article-Display/Article/400022/lab-demonstrates-robotic-ground-refueling-of-aircraft/. Accessed: 2024-06-24.

12. X. Cai. The application of extended kalman filtering based on slam. *Applied and Computational Engineering*, 12, 2023. ISSN 2755-2721. doi: 10.54254/2755-2721/12/20230293.

13. N. Carion, F. Massa, G. Synnaeve, N. Usunier, A. Kirillov, and S. Zagoruyko. End-to-end object detection with transformers. volume 12346 LNCS, 2020. doi: 10.1007/978-3-030-58452-8_13.

14. C.-I. Chen and R. Stettner. Drogue tracking using 3d flash lidar for autonomous aerial refueling. volume 8037, 2011. doi: 10.1117/12.886572.

15. F. Chen, X. Wang, Y. Zhao, S. Lv, and X. Niu. Visual object tracking: A survey. *Computer Vision and Image Understanding*, 222, 9 2022. ISSN 1090235X. doi: 10.1016/j.cviu.2022.103508.

16. Y. Chen, X. Yuan, R. Wu, J. Wang, Q. Hou, and M.-M. Cheng. Yolo-ms: Rethinking multi-scale representation learning for real-time object detection, 2023.

17. G. Cheng, X. Yuan, X. Yao, K. Yan, Q. Zeng, X. Xie, and J. Han. Towards large-scale small object detection: Survey and benchmarks. *IEEE Transactions on Pattern Analysis and Machine Intelligence*, 45, 2023. ISSN 19393539. doi: 10.1109/TPAMI.2023.3290594.

18. O. Cokorilo, S. Gvozdenovic, L. Vasov, and P. Mirosavljevic. Costs of unsafety in aviation. *Technological and Economic Development of Economy - TECHNOL ECON DEV ECON*, 16:188–201, 06 2010. doi: 10.3846/tede.2010.12.

19. N. Cummins. How is an aircraft refueled? 9 2020. URL https://simpleflying.com/how-is-an-aircraft-refuled/.

20. J. Dai, Y. Li, K. He, and J. Sun. R-FCN: object detection via region-based fully convolutional networks. *CoRR*, abs/1605.06409, 2016. URL http://arxiv.org/abs/1605.06409.

21. T. Diwan, G. Anirudh, and J. V. Tembhurne. Object detection using yolo: challenges, architectural successors, datasets and applications. *Multimedia Tools and Applications*, 82, 2023. ISSN 15737721. doi: 10.1007/s11042-022-13644-y.

22. H. Face. Object detection leaderboard, 2023. URL https://huggingface.co/blog/object-detection-leaderboard. Accessed: 2024-06-17.

23. W. Falcon and The PyTorch Lightning team. PyTorch Lightning, Mar. 2019. URL https://github.com/Lightning-AI/lightning.

24. H. Fan, L. Zhu, and Y. Yang. Cubic lstms for video prediction. page 8263 – 8270, 2019. URL https://www.scopus.com/inward/record.uri?eid=2-s2.0-85085021761&partnerID=40&md5=5ef1e8834ec46834bbb53bbcf11720c9. Cited by: 41.

25. J. Feng, Y. Li, C. Zhang, F. Sun, F. Meng, A. Guo, and D. Jin. Deepmove: Predicting human mobility with attentional recurrent networks. 2018. doi: 10.1145/3178876.3186058.

26. N. Ficken. Concept demonstration explores robotic aviation refueling system, July 18 2017. URL https://www.army.mil/article/190980/concept_demonstration_explores_robotic_aviation_refueling_system. Accessed: 2024-06-24.

27. Z. Ge, S. Liu, F. Wang, Z. Li, and J. Sun. YOLOX: exceeding YOLO series in 2021. *CoRR*, abs/2107.08430, 2021. URL https://arxiv.org/abs/2107.08430.

28. A. Ghosh. Yolov10: The dual-head og of yolo series, 2024. URL https://learnopencv.com/yolov10/. Accessed: 2024-06-24.

29. R. B. Girshick. Fast R-CNN. *CoRR*, abs/1504.08083, 2015. URL http://arxiv.org/abs/1504.08083.

30. R. B. Girshick, J. Donahue, T. Darrell, and J. Malik. Rich feature hierarchies for accurate object detection and semantic segmentation. *CoRR*, abs/1311.2524, 2013. URL http://arxiv.org/abs/1311.2524.

31. K. Gong, B. Liu, X. Xu, Y. Xu, Y. He, Z. Zhang, and J. Rasol. Research of an unmanned aerial vehicle autonomous aerial refueling docking method based on binocular vision. *Drones*, 7, 2023. ISSN 2504446X. doi: 10.3390/drones7070433.

32. Intel. Intel realsense depth camera d435, 2024. URL https://www.intelrealsense.com/depth-camera-d435/. Accessed: 2024-06-24.

33. G. Jocher. Yolov5 release v7.0, 2022. URL https://github.com/ultralytics/yolov5/tree/v7.0.

34. G. Jocher. Yolov8, 2023. URL https://github.com/ultralytics/ultralytics/tree/main.

35. G. Jocher, A. Chaurasia, and J. Qiu. Ultralytics YOLO, Jan. 2023. URL https://github.com/ultralytics/ultralytics.

36. R. E. Kalman. A new approach to linear filtering and prediction problems, 1960.

37. J. Kang, S. Tariq, H. Oh, and S. Woo. A survey of deep learning-based object detection methods and datasets for overhead imagery. *IEEE Access*, 10:1–1, 01 2022. doi: 10.1109/ACCESS.2022.3149052.

38. M. M. Karim, Z. Yin, and R. Qin. An attention-guided multistream feature fusion network for early localization of risky traffic agents in driving videos. *IEEE Transactions on Intelligent Vehicles*, pages 1–12, 2023. doi: 10.1109/TIV.2023.3275543.

39. M. M. Karim, R. Qin, and Y. Wang. Fusion-gru: A deep learning model for future bounding box prediction of traffic agents in risky driving videos. *Transportation Research Record*, 2024. ISSN 21694052. doi: 10.1177/03611981241230540.

40. D. Kingma and J. Ba. Adam: A method for stochastic optimization. In *International Conference on Learning Representations (ICLR)*, San Diega, CA, USA, 2015.

41. B. Kuang, S. Barnes, G. Tang, and K. Jenkins. A dataset for autonomous aircraft refueling on the ground (agr). 2023. doi: 10.1109/ICAC57885.2023.10275212.

42. J. Kugarajeevan, T. Kokul, A. Ramanan, and S. Fernando. Transformers in single object tracking: An experimental survey. *IEEE Access*, 11, 2023. ISSN 21693536. doi: 10.1109/ACCESS.2023.3298440.

43. D. Lee, M. Choi, and J. Lee. Prediction of head movement in 360-degree videos using attention model. *Sensors*, 21(11), 2021. ISSN 1424-8220. doi: 10.3390/s21113678. URL https://www.mdpi.com/1424-8220/21/11/3678.

44. W. C. Lee, Y. B. Jeon, S. S. Han, and C. S. Jeong. Position prediction in space system for vehicles using artificial intelligence. *Symmetry*, 14, 2022. ISSN 20738994. doi: 10.3390/sym14061151.

45. C. Li, L. Li, Y. Geng, H. Jiang, M. Cheng, B. Zhang, Z. Ke, X. Xu, and X. Chu. Yolov6 v3.0: A full-scale reloading, 2023.

46. T.-Y. Lin, P. Goyal, R. Girshick, K. He, and P. Dollár. Focal loss for dense object detection, 2018.

47. K. Liu, L. Chen, and X. Liu. Research on application of frontier technologies at smart airport. In J. Zeng, P. Qin, W. Jing, X. Song, and Z. Lu, editors, *Data Science*, pages 319–330, Singapore, 2021. Springer Singapore. ISBN 978-981-16-5943-0.

48. S. Liu, D. Liu, G. Srivastava, D. Połap, and M. Woźniak. Overview and methods of correlation filter algorithms in object tracking. *Complex and Intelligent Systems*, 7, 2021. ISSN 21986053. doi: 10.1007/s40747-020-00161-4.

49. W. Liu, D. Anguelov, D. Erhan, C. Szegedy, S. E. Reed, C. Fu, and A. C. Berg. SSD: single shot multibox detector. *CoRR*, abs/1512.02325, 2015. URL http://arxiv.org/abs/1512.02325.

50. S. Malla, I. Dwivedi, B. Dariush, and C. Choi. Nemo: Future object localization using noisy ego priors. 2019.

51. M. D. L. Olja Čokorilo and G. Dell'Acqua. Aircraft safety analysis using clustering algorithms. *Journal of Risk Research*, 17(10):1325–1340, 2014. doi: 10.1080/13669877.2013.879493. URL https://doi.org/10.1080/13669877.2013.879493.

52. W. Oueslati, S. Tahri, H. Limam, and J. Akaichi. A new approach for predicting the future position of a moving object: Hurricanes' case study. *Applied Artificial Intelligence*, 35, 2021. ISSN 10876545. doi: 10.1080/08839514.2021.1998299.

53. E. Plaza and M. Santos. Knowledge based approach to ground refuelling optimization of commercial airplanes. *Expert Systems*, 38, 2021. ISSN 14680394. doi: 10.1111/exsy.12631.

54. P. Rawat and M. D. Sawale. Gaussian kernel filtering for video stabilization, 2017.

55. J. Redmon and A. Farhadi. YOLO9000: better, faster, stronger. *CoRR*, abs/1612.08242, 2016. URL http://arxiv.org/abs/1612.08242.

56. J. Redmon, S. K. Divvala, R. B. Girshick, and A. Farhadi. You only look once: Unified, real-time object detection. *CoRR*, abs/1506.02640, 2015. URL http://arxiv.org/abs/1506.02640.

57. S. Ren, K. He, R. Girshick, and J. Sun. Faster r-cnn: Towards real-time object detection with region proposal networks. *IEEE Transactions on Pattern Analysis and Machine Intelligence*, 39, 2017. ISSN 01628828. doi: 10.1109/TPAMI.2016.2577031.

58. R. Sati, S. Singh, and R. Yadav. Aircraft fuel system: design, components, and safety. *International Journal of Aerospace Engineering*, 2019:1–12, 2019. doi: 10.1155/2019/6943787.

59. A. Savitzky and M. J. E. Golay. Smoothing and differentiation of data by simplified least squares procedures. *Analytical Chemistry*, 36(8):1627–1639, 1964. doi: 10.1021/ac60214a047.

60. R. W. Schafer. What is a savitzky-golay filter? [lecture notes]. *IEEE Signal Processing Magazine*, 28(4):111–117, 2011. doi: 10.1109/MSP.2011.941097.

61. E. R. Schultz. Robotic systems for aircraft servicing/maintenance. *IEEE Aerospace and Electronic Systems Magazine*, 1, 1986. ISSN 08858985. doi: 10.1109/MAES.1986.5005018.

62. X. Shi, Z. Chen, H. Wang, D. Yeung, W. Wong, and W. Woo. Convolutional LSTM network: A machine learning approach for precipitation nowcasting. *CoRR*, abs/1506.04214, 2015. URL http://arxiv.org/abs/1506.04214.

63. S. W. Smith. The scientist and engineer's guide to digital signal processing, 1999. URL https://www.analog.com/media/en/technical-documentation/dsp-book/dsp_book_Ch15.pdf. Chapter 15.

64. N. Srivastava, E. Mansimov, and R. Salakhutdinov. Unsupervised learning of video representations using lstms. *CoRR*, abs/1502.04681, 2015. URL http://arxiv.org/abs/1502.04681.

65. O. Styles, T. Guha, and V. Sanchez. Multiple object forecasting: Predicting future object locations in diverse environments, 2020.

66. A. Wang, H. Chen, L. Liu, K. Chen, Z. Lin, J. Han, and G. Ding. Yolov10: Real-time end-to-end object detection, 2024.

67. C. Wang, W. He, Y. Nie, J. Guo, C. Liu, K. Han, and Y. Wang. Gold-yolo: Efficient object detector via gather-and-distribute mechanism, 2023.

68. C.-Y. Wang, I.-H. Yeh, and H.-Y. M. Liao. Yolov9: Learning what you want to learn using programmable gradient information, 2024.

69. X. Wang, X. Dong, X. Kong, J. Li, and B. Zhang. Drogue detection for autonomous aerial refueling based on convolutional neural networks. *Chinese Journal of Aeronautics*, 30, 2017. ISSN 10009361. doi: 10.1016/j.cja.2016.12.022.

70. J. Wu and S. Xu. From point to region: Accurate and efficient hierarchical small object detection in low-resolution remote sensing images. *Remote Sensing*, 13, 2021. ISSN 20724292. doi: 10.3390/rs13132620.

71. S. Xu, X. Wang, W. Lv, Q. Chang, C. Cui, K. Deng, G. Wang, Q. Dang, S. Wei, Y. Du, and B. Lai. Pp-yoloe: An evolved version of yolo, 2022.

72. X. Xu, Y. Jiang, W. Chen, Y. Huang, Y. Zhang, and X. Sun. Damo-yolo : A report on real-time object detection design, 2023.

73. Y. Yao, M. Xu, C. Choi, D. J. Crandall, E. M. Atkins, and B. Dariush. Egocentric vision-based future vehicle localization for intelligent driving assistance systems. In *International Conference on Robotics and Automation*, 2019.

74. T. Ye, W. Qin, Z. Zhao, X. Gao, X. Deng, and Y. Ouyang. Real-time object detection network in uav-vision based on cnn and transformer. *IEEE Transactions on Instrumentation and Measurement*, 72, 2023. ISSN 15579662. doi: 10.1109/TIM.2023.3241825.

75. S. Yildirim and Z. A. Rana. Reducing the reality gap using hybrid data for real-time autonomous operations. *Mathematics*, 11, 2023. ISSN 22277390. doi: 10.3390/math11071696.

76. S. Yildirim, Z. Rana, and G. Tang. Autonomous ground refuelling approach for civil aircrafts using computer vision and robotics. volume 2021-October, 2021. doi: 10.1109/DASC52595.2021.9594312.

77. S. Yildirim, Z. A. Rana, and G. Tang. Development of vision guided real-time trajectory planning system for autonomous ground refuelling operations using hybrid dataset. 2023. doi: 10.2514/6.2023-1148.

78. S. S. A. Zaidi, M. S. Ansari, A. Aslam, N. Kanwal, M. Asghar, and B. Lee. A survey of modern deep learning based object detection models, 2022. ISSN 10512004.

79. Y. Zhang, T. Wang, K. Liu, B. Zhang, and L. Chen. Recent advances of single-object tracking methods: A brief survey. *Neurocomputing*, 455, 2021. ISSN 18728286. doi: 10.1016/j.neucom.2021.05.011.

80. Z. Zhong, D. Li, H. Wang, and Z. Su. Drogue position and tracking with machine vision for autonomous air refueling based on ekf. volume 2, 2017. doi: 10.1109/IHMSC.2017.151.